Author(s): Xiao, Yihua; Carena, Luca; Näsi, Marja-Terttu; Vähätalo, Anssi V.

Title: Superoxide-driven autocatalytic dark production of hydroxyl radicals in the presence of complexes of natural dissolved organic matter and iron

Year: 2020

Version: Accepted version (Final draft)

Please cite the original version:

Xiao, Y., Carena, L., Näsi, M.-T., & Vähätalo, A. V. (2020). Superoxide-driven autocatalytic dark production of hydroxyl radicals in the presence of complexes of natural dissolved organic matter and iron. Water Research, 177, Article 115782. https://doi.org/10.1016/j.watres.2020.115782

Journal Pre-proof

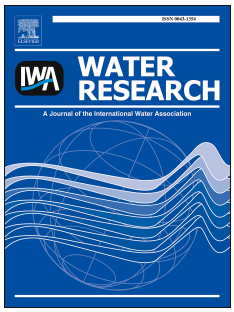

Superoxide-driven autocatalytic dark production of hydroxyl radicals in the presence of complexes of natural dissolved organic matter and iron

Yihua Xiao, Luca Carena, Marja-Terttu Näsi, Anssi V. Vähätalo

PII: S0043-1354(20)30319-5

DOI: https://doi.org/10.1016/j.watres.2020.115782

Reference: WR 115782

To appear in: *Water Research*

Received Date: 22 November 2019

Revised Date: 31 March 2020

Accepted Date: 1 April 2020

Please cite this article as: Xiao, Y., Carena, L., Näsi, M.-T., Vähätalo, A.V., Superoxide-driven autocatalytic dark production of hydroxyl radicals in the presence of complexes of natural dissolved organic matter and iron, *Water Research* (2020), doi: https://doi.org/10.1016/j.watres.2020.115782.

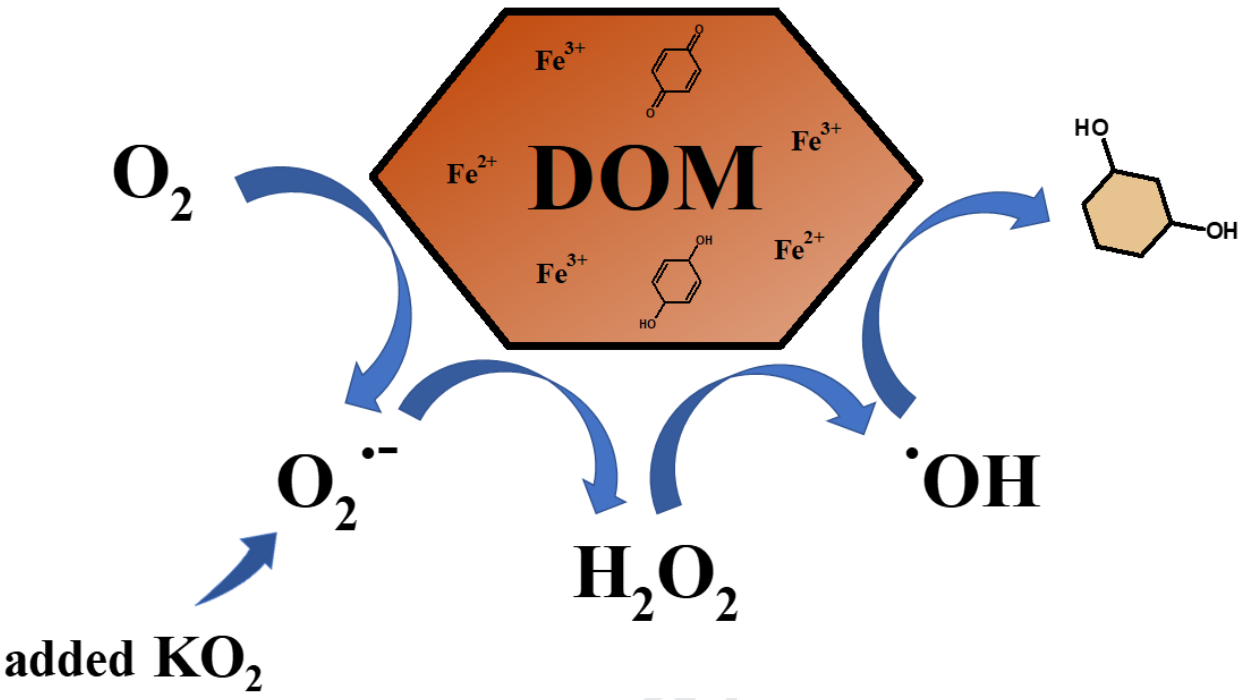
O_2
Fe^{3+}
Fe^{2+}
DOM
Fe^{3+}
Fe^{3+}
Fe^{2+}
HO
OH
HO
OH
$O_2^{\bullet-}$
H_2O_2
$^{\bullet}OH$
added KO_2

Superoxide-driven autocatalytic dark production of hydroxyl radicals in the presence of complexes of natural dissolved organic matter and iron

Yihua Xiao[1,2*], *Luca Carena*[3], *Marja-Terttu Näsi*[1], *Anssi V. Vähätalo*[1]

[1]Department of Biological and Environmental Science, University of Jyväskylä, 40014 Jyväskylä, Finland

[2]School of Environmental & Municipal Engineering, Qingdao University of Technology, 266033 Qingdao, China

[3]Dipartimento di Chimica, Università di Torino, Via Pietro Giuria 5, 10125 Torino, Italy

*Corresponding author: yihua.y.xiao@jyu.fi

Abstract

We introduced superoxide as potassium superoxide (KO_2) to artificial lake water containing dissolved organic matter (DOM) without or with introduced ferric iron complexes (DOM-Fe), and monitored the production rate of hydroxyl radicals as well as changes in the absorption and fluorescence properties of DOM. The introduction of KO_2 decreased the absorption by DOM but increased the spectral slope coefficient of DOM more with complexed ferric Fe than without it. The introduction of KO_2 increased the fluorescence of humic-like components in DOM without introduced ferric Fe but resulted in the loss of fluorescence in DOM with introduced ferric Fe. A single introduction of 13 µmol L^{-1} KO_2 produced 10 µmol L^{-1} and 104 µmol L^{-1} hydroxyl radicals during a week-long experiment without and with the introduced DOM-Fe complexes, respectively. The production rate of hydroxyl radicals decreased exponentially with time but levelled off and continued several days in DOM with introduced ferric Fe. These findings suggest that in the presence of DOM-Fe complexes, superoxide can trigger an autocatalytic Fenton reaction that produces hydroxyl radicals and breaks down DOM.

Keywords: dissolved organic matter, iron, superoxide, hydroxyl radicals, production rate, absorption

1 Introduction

Dissolved organic matter (DOM) is a heterogeneous mixture of organic compounds and plays important roles in natural and engineered systems. In soils and freshwaters, the majority of DOM consists of humic substances that primarily originate from terrestrial plant litter after biotic and abiotic transformations (Piccolo, 1996; Tranvik, 1988). Humic DOM binds ferric iron, Fe(III), into complexes, DOM-Fe(III), and keeps poorly soluble Fe(III) in dissolved form (Fujii et al., 2014). Humic DOM contains aromatic and quinone-like moieties, which occur in three redox-states (quinones, semiquinones and hydroquinones) and can mediate reactions between electron donors and acceptors (Aeschbacher et al., 2010; Chen & Pignatello, 1997; Garg et al., 2018; Yuan et al., 2016).

The enzymatic hydrolysis of humic DOM and its intracellular metabolism is inefficient, because the large size of molecular aggregates, chemical heterogeneity, and non-hydrolysable bonds limit the microbial transformation of humic DOM (Arnosti, 2004). Abiotic photochemical reactions mineralize humic DOM and account for one tenth of CO_2 emissions in freshwaters (Aarnos et al., 2018; Koehler et al., 2014). The remaining 90% of DOM is mineralized through mechanisms that are poorly known.

Extracellular reactions between DOM and reactive oxygen species (ROS) can explain a part of DOM transformations (Mostovaya et al., 2017; Page et al., 2012; Trusiak et al., 2018; Waggoner et al., 2017). The first step in the formation of ROS is a one-electron reduction of O_2 to superoxide ($O_2^{\bullet-}$). Numerous processes produce $O_2^{\bullet-}$: (i) photochemical reactions (Micinski et al., 1993; Fujii & Otani, 2017; Zhang & Blough, 2016; Text SIV in supporting information (SI)), (ii) abiotic dark oxidation of reduced metals or organic matter (Garg et al., 2018; Gil-Lozano et al., 2017; Page et al., 2012; Yuan et al., 2016) and (iii) biological processes both in light and dark (Diaz et al., 2013; Diaz & Plummer, 2018; Imlay, 2004; Zhang et al., 2016). $O_2^{\bullet-}$ reacts with the redox-active metals (e.g., Fe and copper) and

quinone-like moieties of DOM, but it has otherwise limited reactivity with aqueous DOM (Garg et al., 2011, 2018; Hayyan et al., 2016; Yuan et al., 2016).

$O_2^{\bullet-}$ can be reduced further to hydrogen peroxide (H_2O_2) and hydroxyl radicals ($^{\bullet}OH$). Bimolecular disproportionation and the disproportionation catalyzed by reduced metals or DOM transform $O_2^{\bullet-}$ to H_2O_2 (Goldstone & Voelker, 2000; Ma et al., 2010). $O_2^{\bullet-}$ can reduce DOM-Fe(III) to DOM-Fe(II) (Rose & Waite, 2005). DOM-Fe(II) as well as inorganic Fe(II) can react with H_2O_2 through the Fenton reaction and produce highly reactive $^{\bullet}OH$ that breaks down DOM (Southworth & Voelker, 2003; Voelker et al., 1997).

$$H_2O_2 + \text{DOM-Fe(II)} \rightarrow {}^{\bullet}OH + OH^- + \text{DOM-Fe(III)} \qquad \text{Eq. 1}$$

According to the stoichiometry of the Fenton reaction (Eq. 1), the Fe(III)-catalyzed production of $^{\bullet}OH$ requires three $O_2^{\bullet-}$ radicals, two for the formation of H_2O_2 and one for the formation of DOM-Fe(II). However, the stoichiometry of the Fenton reaction ($^{\bullet}OH$-to-$O_2^{\bullet-}$ ratio = 0.33) ignores a well-known fact that $^{\bullet}OH$ generates radical species that can regenerate the Fenton reactants and autocatalyze the Fenton reaction (e.g., Chen & Pignatello, 1997; Gil-Lozano et al., 2017). The degree of autocatalysis is poorly known, although it has high importance when the efficiency of the Fenton reaction is evaluated in natural or engineered systems.

The present study estimates the dark production rates of $^{\bullet}OH$ in artificial lake water from $O_2^{\bullet-}$ (introduced as potassium superoxide, KO_2) in the presence of DOM with or without introduced Fe(III). The production rates of $^{\bullet}OH$ were quantified from the reaction between $^{\bullet}OH$ and coumarin (Louit et al., 2005) and after accounting for the major scavengers of $^{\bullet}OH$ in the artificial lake water. In this study we demonstrate that the cumulative production of $^{\bullet}OH$ from $O_2^{\bullet-}$ in a-week-long experiment exceeds the $^{\bullet}OH$ yield of the Fenton reaction by several folds and extensively modifies the spectroscopic properties of DOM.

2 Materials and methods

2.1 Materials and reagents

DOM was extracted from a water sample collected during the fall turnover of Lake Valkea-Kotinen in southern Finland. This small headwater lake is acidic (pH 5.4) with high concentration of DOC (10–12 mg DOC L^{-1} = ~20 mg DOM L^{-1}) and total Fe (~5 µM; Einola et al., 2011; Vähätalo et al., 2003). In Lake Valkea-Kotinen, the mean molecular mass of DOM is 1130–4000 g mol^{-1}, the content of humic substances and aromatic groups is 75% and 45–67%, respectively (Vogt et al., 2004).

The extraction of DOM followed the method by Dittmar et al. (2008) but included an addition of 0.01 M sodium fluoride (NaF, Sigma-Aldrich) in filtered (<0.2 µm) and acidified (pH 2) lake water. At pH 2, Fe(III) binds poorly on DOM and preferentially forms ferric fluoride complex (Gao & Zepp, 1998). Ferric fluoride and fluoride ions were rinsed out of the column with 0.01 M HCl (Dittmar et al. 2008) to yield extracted DOM with a very low content of fluoride and Fe. The extraction removed 96.6% of Fe from lake water and the DOM extracts contained 8.5 nmol Fe/mg DOM (Table 1). The chemicals (>97% pure) were bought from Sigma Aldrich. Iron(III) chloride hexahydrate ($FeCl_3 \cdot 6H_2O$) and KO_2 were the sources of Fe(III) and $O_2^{\bullet-}$, respectively. Coumarin and 7OH-coumarin were the probes for $^{\bullet}OH$ (Burgos Castillo et al., 2018). The aqueous solutions were prepared in ultrapure water (resistivity 18 MΩ·cm; SG ultrapure water system, SG WATER), but were later modified to artificial lake water by a salt solution mixture (Table S1). Glassware was soaked overnight in 0.1 M HCl and carefully rinsed with ultrapure water six times prior to use.

2.2 Experimental setup

The experiment consisted of four treatments prepared in triplicates (Table 1):

1) "control" – extracted DOM (8.5 nmol Fe/mg DOM) dissolved in artificial lake water;
2) "KO_2" – like (1) but with introduced KO_2;

3) "Fe" – like (1) but Fe(III) was introduced as DOM-Fe(III) (1000 nmol Fe(III)/mg DOM);

4) "Fe + KO_2" – a combination of (2) and (3).

For the preparation of DOM-Fe(III), the acidic (pH 2) DOM solution (50 mg L^{-1} in ultrapure water) received 1 mM Fe(III) and was titrated to pH 5 with NaOH and HCl, approximating the ambient pH of Lake Valkea-Kotinen. During the titration, the binding sites of DOM suppressed the hydrolysis of ferric Fe and DOM-Fe(III) was formed (Karlsson & Persson, 2012). According to an equilibrium speciation model (Visual Minteq 3.1), the DOM extract was able to bind Fe(III) entirely and accordingly visual precipitates were absent at any phase of the experiment. The "control" and "KO_2" treatments were titrated in the same way but without the introduced Fe. All treatments received the stock solution of coumarin to the final concentration of 10 µM (Table 1) and inorganic component of artificial lake water (Table S1).

The "KO_2" and "Fe + KO_2" treatments received an alkaline solution of KO_2 (2 g KO_2 in 100 mL 0.05 M NaOH) to a 13 µM final concentration (Table 1). Similar magnitudes of $O_2^{\bullet-}$ form instantly during the oxidation of reduced organic matter or metals (Liao et al., 2019; Minella et al., 2015; Page et al., 2013; Trusiak et al., 2018; Zhang & Yuan, 2017), with a few days of microbial metabolism (Zhang et al., 2016) or with 0.17–few days of solar irradiation depending on water quality (Cooper & Zika, 1983; Micinski et al., 1993; Text SIV in SI). The introduction of KO_2 increased the pH of non-buffered artificial lake water to 12.2, where the reduction rate of DOM-Fe(III) to DOM-Fe(II) by $O_2^{\bullet-}$ is faster than bimolecular disproportionation of $O_2^{\bullet-}$ (see Text SI in SI). The reaction medium was titrated back to pH 5 with HCl. Finally, all treatments were incubated at 20 °C in the dark with a headspace of air.

2.3 UV-Vis spectral analysis

After 26 h and a week (168 h) of incubation, the absorbance of chromophoric DOM

(CDOM) was measured with a UV-Vis spectrometer (Lambda 850, PerkinElmer) from 200 nm to 700 nm at 1 nm intervals. The absorption coefficient was calculated as,

$a_\lambda = 2.303 \times A_\lambda / L$ Eq. 2,

where a_λ (m^{-1}) is the absorption coefficient at wavelength λ, A_λ (unitless) is absorbance, and L is the path length of the cuvette (L = 0.01 m). The changes in a_λ were quantified at 410 nm as a_{410}, an indicator of water color (Hongve et al., 2004). The spectral slope coefficient ($S_{275\text{-}295}$), which indicates the molecular mass of DOM, was calculated from ln-transformed absorption coefficient between 275 nm and 295 nm (Helms et al., 2008).

2.4 Fluorescence analysis and PARAFAC

Samples for fluorescence analysis were stored at 4 °C after collection and measured within 3 weeks. Fluorescence EEMs were measured with a LS 55 luminescence spectrometer (PerkinElmer). The samples were scanned with an excitation wavelength (Ex) from 240 nm to 450 nm at 5 nm intervals and emission wavelength (Em) from 300 nm to 600 nm with 0.5 nm intervals. The slit width for both Ex and Em was set to 5 nm. Blank and Raman samples from ultrapure water were measured prior to actual samples (Murphy et al., 2003).

PARAllel FACtor analysis (PARAFAC) was run in Matlab R2015b (Mathworks, USA) using the drEEM toolbox (version 0.3.0). The raw EEM dataset (n = 48) was corrected for spectral bias, inner filter effects and background signals (measured with ultrapure water). In the end, all EEMs were normalized to the area of Raman peak collected with ultrapure water at Ex = 275 nm to compensate for daily fluctuations in lamp intensity (Kothawala et al., 2016; Murphy et al., 2013). The fluorescent components were validated with multiple split-half tests. The validation was constrained by a Tucker congruence coefficient (TCC >0.95). Finally, the maximum fluorescence intensities (F_{max}, in Raman unit, R.U.) of components were reported.

2.5 Calculations of the cumulative production of •OH radicals

The samples for the quantification of coumarin and 7OH-coumarin were collected at 0, 3, 6, 20, 26, and 168 h. These samples were frozen immediately after collection and analyzed later. Coumarin and 7OH-coumarin were measured by high performance liquid chromatography (HPLC) equipped with UV-Vis absorbance and fluorescence detectors (Louit et al., 2005). The quantification of the two compounds was carried out by means of the UV-Vis absorbance detector for coumarin (absorption wavelength = 280 nm) and fluorescence detector for 7OH-coumarin (excitation wavelength = 320 nm; emission wavelength = 450 nm). The Text SII in SI reports the details of HPLC technique.

The formation rates of •OH were quantified from the reaction between coumarin and •OH. This reaction has a second-order rate constant of 5.6×10^9 M^{-1} s^{-1} and produces a few hydroxycoumarin isomers, including 7OH-coumarin with a yield of 0.047 (Burgos Castillo et al., 2018). We calculated the production rates of •OH along the course of the experiment by quantifying periodically the concentrations of 7OH-coumarin and coumarin as well as accounting for the scavenging of •OH by DOM, Cl^-, HCO_3^-, coumarin and 7OH-coumarin. The calculations assumed a steady-state between the scavenging and the formation rate of •OH. The production rates of •OH radicals were integrated over the course of the experiment for the cumulative production of •OH. The detailed procedure for calculations is described in the SI.

2.6 Statistical analyses

The statistical difference between the triplicated treatments and control (DOM alone treatment) was assessed using paired *t* tests with two-tailed distributions. The significance level was set at $P < 0.05$.

3 Results

3.1 Changes in absorption spectra

The introduction of KO_2 did not change the absorption coefficient a_{410} in an early phase of the experiment (at 26 h) but decreased it by 25% by the end of the experiment (at 168 h) compared to DOM in artificial lake water without KO_2 ("control" vs "KO_2", Figure 1a). In the "Fe" treatment, the introduced DOM-Fe(III) consistently kept a_{410} at a higher level than in the control (Figure 1a). When introduced with DOM-Fe(III), KO_2 decreased a_{410} by 18% already at 26 h and by 66% over the entire experiment compared to the control ("Fe + KO_2", Figure 1a).

In comparison with the control treatment, KO_2 increased the spectral slope coefficient ($S_{275\text{-}295}$), while DOM-Fe(III) decreased it (Figure 1b). When introduced with Fe, KO_2 increased $S_{275\text{-}295}$ by 20% at 26 h and by 54% at the end of the experiment (Figure 1b).

3.2 Changes in fluorescent intensities of PARAFAC components

The four components of fluorescent DOM identified by the EEM-PARAFAC associated with humic substances (Comp 1–2, Figure 2 and Table S2), 7OH-coumarin (Comp 3; Figure S1) and protein-like DOM (Comp 4, Figure 2 and Table S2). After 168 h, the introduction of KO_2 had increased the fluorescence of humic-like components 1 and 2 by 39% and 18%, respectively, in comparison to the control treatment ("KO_2", Figure 3). The added associated Fe(III) quenched the fluorescence of humic-like components 1–2 ("Fe", Figure 3). In the presence of DOM-Fe(III), KO_2 reduced the fluorescence of components 1–2 relative to the control treatment and decreased the fluorescence of component 4 to negligible level ("Fe + KO_2", Figure 3). Component 3 was detected in all treatments (Figure 3) indicating that $^{\bullet}OH$ radicals transformed coumarin (Table 1) into 7OH-coumarin, as explained in the following section.

3.3 Production of $^{\bullet}OH$

The formation rate of $^{\bullet}OH$, $R_f^{\bullet OH}(t)$, was assessed from the measured concentrations of coumarin and 7OH-coumarin (Figure SIII-1&2) accounting for the other scavengers of $^{\bullet}OH$ as described in the Text SIII in SI. In the beginning of the experiment, $R_f^{\bullet OH}(t_0)$ was 0.0031–0.0034 nM s^{-1} in the "Fe" treatment and the control, which did not receive KO_2 (Figure 4; Table SIII-1). The introduction of KO_2 resulted in $R_f^{\bullet OH}(t_0)$ of 0.039 nM s^{-1} and 1.14 nM s^{-1} in the "KO_2" and "KO_2 + Fe"-treatments, respectively (Figure 4; Table SIII-1). In the "KO_2 + Fe" treatment, the measured $R_f^{\bullet OH}(t_0)$ was nearly identical to the corresponding rate of 1.05 nM s^{-1} calculated based on a simple kinetic model (Figure SI-2). Briefly, the calculated rates are based on the kinetics for the following sequence of reactions: (i) the reduction of DOM-Fe(III) to 13 µM DOM-Fe(II) by $O_2^{\bullet-}$, (ii) the reduction of O_2 to $O_2^{\bullet-}$ by DOM-Fe(II), (iii) the disproportionation of $O_2^{\bullet-}$ to H_2O_2 and (iv) the Fenton reaction (Eq. 1) between H_2O_2 and DOM-Fe(II). The good match between the measured and the calculated $R_f^{\bullet OH}(t_0)$ in the "KO_2 + Fe" treatment suggest that, (i) $O_2^{\bullet-}$ induced the formation of $^{\bullet}OH$ in the presence of DOM-Fe(III) and (ii) the reaction stoichiometry (e.g., $^{\bullet}OH$-to-$O_2^{\bullet-}$ ratio = 0.33 of Eq. 1) described the measured initial rates well.

The formation rates of $^{\bullet}OH$ decreased exponentially with time in all treatments, and after 10 h levelled at 0.15 nM s^{-1} in the "KO_2 + Fe" treatment (Figure 4, Table SIII-1). In the "KO_2 + Fe" treatment, the prolonged formation of $^{\bullet}OH$ is consistent with the changes in DOM that took place mostly after 26 h (Figure 1), but inconsistent with a simple kinetic model (Text SI-3). The simple kinetic model incorrectly suggests the depletion of $R_f^{\bullet OH}(t)$ within a few minutes (Text SI-3) in contrast to the measured $R_f^{\bullet OH}(t)$, which lasted tens of hours (Figure 4).

The cumulative production of $^{\bullet}OH$ was computed as the integral of $R_f^{\bullet OH}(t)$ for the

first 10 hours or for the entire length of the experiment (168 h, Table 2, Eq. SIII-1). In all treatments, the majority of $^{\bullet}OH$ was produced after 10 h (Table 2). In the treatments with introduced KO_2, the cumulative production of $^{\bullet}OH$ was 9.9 and 104 µM in the "KO_2" and "KO_2 + Fe" treatments, respectively, over the entire length of the experiment (Table 2). The yields of $^{\bullet}OH$ per introduced 13 µM KO_2 were 0.76 $^{\bullet}OH/O_2^{\bullet-}$ and 8 $^{\bullet}OH/O_2^{\bullet-}$ in the "KO_2" and "KO_2 + Fe" treatments, respectively. The measured yields exceeded the stoichiometric yield (0.33 $^{\bullet}OH/O_2^{\bullet-}$ in Eq. 1) by a factor of 2.3 and 24 in the "KO_2" and "KO_2 + Fe" treatments, respectively, and indicated an autocatalytic formation of $^{\bullet}OH$ from $O_2^{\bullet-}$ in the presence of DOM-Fe.

4 Discussion

4.1 $^{\bullet}OH$ production

As explained in the Method-section 2.2, the amount of introduced $O_2^{\bullet-}$ in this study is environmentally relevant but here we compare the cumulative productions of $^{\bullet}OH$ (0.23–104 µM) in our week-long experiment to those reported earlier. An oxidation of reduced DOM or metals produces $^{\bullet}OH$. For example, the oxidation of Arctic surface and soil waters produce 0.2–4.5 µM $^{\bullet}OH$ over 24 hour oxidation (Page et al., 2013); the oxidation of hypolimnetic water accumulatively produces 0.2–4.5 µM $^{\bullet}OH$ (Minella et al., 2015); the oxidation of pyrite can produce 7.5–135 µM $^{\bullet}OH$ within 7 hours (Zhang & Yuan, 2017); and the oxidation of river sediments can accumulatively produce 57–1479 µmol kg^{-1} $^{\bullet}OH$ within 48 hours (Liao et al., 2019). Thus, the cumulative productions of $^{\bullet}OH$ in this study are broadly similar to those reported earlier from various environmental processes.

4.2 Stoichiometric production of $^{\bullet}OH$ from superoxide and DOM-Fe(III)

In this study, the production of $^{\bullet}OH$ is orders of magnitude larger in the presence than

the absence of introduced KO_2, therefore, $O_2^{\bullet-}$ is responsible for the extensive production of $^{\bullet}OH$. The reaction pathway from $O_2^{\bullet-}$ to $^{\bullet}OH$ is beyond the scope of the present study, because we did not measure the intermediates such as DOM-Fe(II) or H_2O_2. Our simple kinetic model, however, successfully predicts the measured $R_f^{\bullet OH}(t_0)$ in the "KO_2 + Fe" treatment and may provide a mechanistic explanation for the initial $^{\bullet}OH$ production rates (Text SI). According to this simple model, the reaction pathway starts with the reduction of DOM-Fe(III) to DOM-Fe(II) by $O_2^{\bullet-}$ (Eq. 3, Text SI). Later, bimolecular disproportionation generates H_2O_2 (Eq. 4). At this stage, the reduction of O_2 by DOM-Fe(II) is the source of $O_2^{\bullet-}$ (Text SI). Finally, H_2O_2 reacts with DOM-Fe(II) (Eq. 1, Text SI). The reactive oxygen species can maintain the redox cycling of the iron catalyst and the production of $^{\bullet}OH$ from the oxidant ($H_2O_2 = 2[O_2^{\bullet-} + H^+]$) according to the stoichiometry of the Fenton reaction (Pignatello et al. 2006; Text SI).

$$\text{DOM-Fe(III)} + O_2^{\bullet-} \rightarrow \text{DOM-Fe(II)} + O_2 \qquad \text{Eq.3,}$$

$$O_2^{\bullet-} + HO_2^{\bullet} + H^+ \rightarrow H_2O_2 + O_2 \qquad \text{Eq.4,}$$

DOM facilitates the formation of $^{\bullet}OH$ through the Fenton reaction in many ways (Georgi et al., 2007). When DOM makes complexes with Fe(III) at pH > 3.5, it keeps Fe(III) in soluble reactive form (Zhang & Zhou, 2019). At low pH (for instance, pH = 5 in this study), the deprotonated carboxylic groups of DOM are favorable ligand for Fe(III) and the concentration of a major competing ligand, hydroxyl ion (OH^-), is low (Bhattacharyya et al., 2019; Lee et al., 2019; Neubauer et al., 2013; Zhang & Zhou, 2019). Mildly acidic conditions (like in the present study) are favorable for the Fenton reaction, which breaks down humic substances most efficiently at pH 4–5 rather than in more acidic or basic solutions (Wu et al., 2010). Additionally, H_2O_2 reacts faster with DOM-Fe(II) than with inorganic Fe(II) (Voelker & Sulzberger 1996; Zhang & Zhou, 2019).

4.3 Autocatalysis of the Fenton reaction

In our study, the cumulative production of $^{\bullet}OH$ is larger (0.76–8 $^{\bullet}OH/O_2^{\bullet-}$) than expected from the introduced $O_2^{\bullet-}$ according to the stoichiometry of the Fenton reaction (0.33 $^{\bullet}OH/O_2^{\bullet-}$). The reactions between $^{\bullet}OH$ and the phenolic moieties of DOM can explain the autocatalysis of the Fenton reaction in this study (Voelker & Sulzberger, 1996, Chen & Pignatello, 1997). Those reactions generate hydroquinone-like DOM and $O_2^{\bullet-}$ (Voelker & Sulzberger, 1996, Chen & Pignatello, 1997, Duesterberg & Waite, 2007). The reactions between $^{\bullet}OH$ and phenols have been examined earlier with model compounds (phenol and hydroxybenzoic acid) that mimick the aromatic moieties of DOM (Chen & Pignatello, 1997; Duesterberg & Waite, 2007). Firstly, an addition of $^{\bullet}OH$ to phenol (PhOH) generates a dihydroxycyclohexadienyl radical (HO-$(C_6H_5)^{\bullet}$-OH, Eq.5), which transforms into hydroquinone (HO-Ar-OH) in a reaction that consumes O_2 and generates $O_2^{\bullet-}$ (Eq.6, Chen & Pignatello, 1997; Voelker & Sulzberger, 1996). Secondly, the transformation of hydroquinone to semiquinone radical (HO-Ar-$O^{\bullet}$) reduces DOM-Fe(III) to DOM-Fe(II) (Eq.7, Chen & Pignatello, 1997; Duesterberg & Waite, 2007). Finally, a semiquinone radical reduces another DOM-Fe(III) when undergoing oxidation to quinone (O=Ar=O) (Eq.8, Chen & Pignatello, 1997; Duesterberg & Waite, 2007).

$$PhOH + {}^{\bullet}OH \rightarrow HO\text{-}(C_6H_5)^{\bullet}\text{-}OH \qquad \text{Eq.5,}$$

$$HO\text{-}(C_6H_5)^{\bullet}\text{-}OH + O_2 \rightarrow HO\text{-}Ar\text{-}OH + O_2^{\bullet-} + H^+ \qquad \text{Eq.6,}$$

$$HO\text{-}Ar\text{-}OH + DOM\text{-}Fe(III) \rightarrow HO\text{-}Ar\text{-}O^{\bullet} + DOM\text{-}Fe(II) + H^+ \qquad \text{Eq.7,}$$

$$HO\text{-}Ar\text{-}O^{\bullet} + DOM\text{-}Fe(III) \rightarrow O{=}Ar{=}O + DOM\text{-}Fe(II) + H^+ \qquad \text{Eq.8,}$$

$$2\ DOM\text{-}Fe(II) + 2\ O_2 \rightarrow 2\ DOM\text{-}Fe(III) + 2\ O_2^{\bullet-} \qquad \text{Eq.9,}$$

The four consecutive reactions (Eq. 5–8) described above produce three reducing equivalents ($O_2^{\bullet-}$ and/or DOM-Fe(II)) that re-generate the Fenton reactants and thus the

297 production of $^{\bullet}$OH gets autocatalyzed through the Fenton reaction and DOM oxidation. Note
298 that the net reaction of this process (from Eq.1 to Eq.9, with the exception of Eq.2) is the
299 oxidation of phenol to quinone (Eq.10).

300 $PhOH + O_2 \rightarrow O{=}Ar{=}O + H_2O$ Eq.10,

301 This autocatalysis can continue as long as water contains O_2 and DOM contains
302 aromatic moieties that $^{\bullet}$OH can transform into hydroquinones. In this study, the headspace of
303 air serves as a source of dissolved O_2 to our solutions like the atmosphere is a source of O_2 to
304 surface waters. The high (45–67%) aromaticity of DOM used in this study (Vogt et al., 2004)
305 provides a large reservoir of aromatic moieties that $^{\bullet}$OH can transform into hydroquinones.
306 Because highly aromatic humic substances and Fe are abundant in soils and freshwaters, the
307 potential for the autocatalyzed Fenton reaction is high in these environments.

308 4.4 Fenton reaction without introduced $O_2^{\bullet-}$

309 Our experiments show that even without introduction of $O_2^{\bullet-}$, DOM-Fe can produce
310 hydroxyl radicals at low amounts that are similar to < 0.5 µM $^{\bullet}$OH produced during aeration
311 of Artic surface waters (Page et al., 2012; Trusiak et al., 2018). Since Lake Valkea-Kotinen
312 has typically anoxic hypolimnion in late summer and it is surrounded by peaty soils, the
313 DOM extract used in the present study may contain Fe or quinone-like moieties in a reduced
314 state. The reduced hydroquinone-like moieties or reduced metals (e.g., Fe(II)) associated to
315 DOM can reduce O_2 to $O_2^{\bullet-}$ and initiate the sequence of reactions leading to the Fenton
316 reaction (Garg et al., 2018; Page et al., 2013, 2014). In this study, the external supply of
317 DOM-Fe(III) doubled the $^{\bullet}$OH production compared to DOM extract alone with low content
318 of Fe and further emphasizes the Fenton reaction as a source of $^{\bullet}$OH. Although an abiotic
319 dark formation of $^{\bullet}$OH is low in oxic surface waters without external source of $O_2^{\bullet-}$ (Trusiak
320 et al., 2018; this study), an episodic mixing of reduced DOM or redox sensitive metals to an

321 oxic environment can promote an extensive production of $^{\bullet}OH$ (Minella et al., 2015; Page et
322 al., 2012, 2013; Trusiak et al., 2018).

323 4.5 Effects of $O_2^{\bullet-}$ and Fe on the absorption spectra of CDOM

324 In this study, the introduction of external $O_2^{\bullet-}$ eventually led to a CDOM breakdown
325 and increased the value of $S_{275\text{-}295}$ (Figure 1). These changes in CDOM are related to the
326 produced amount of $^{\bullet}OH$ radicals and indicate that $^{\bullet}OH$ rather than $O_2^{\bullet-}$ breaks down DOM
327 (Goldstone et al., 2002; Pignatello et al., 2006; Rush & Bielski, 2005; Waggoner et al., 2017;
328 Wu et al., 2010; this study). The changes in CDOM found in this study indicate a breakdown
329 of DOM into smaller less aromatic molecules (Helms et al., 2008) as found earlier in the
330 reactions between DOM and $^{\bullet}OH$ (Goldstone et al., 2002; Pignatello et al., 2006).

331 4.6 Effects of $O_2^{\bullet-}$ and Fe on the fluorescence spectra of CDOM

332 In our study, the introduction of KO_2 without external supply of Fe(III) increases the
333 fluorescence of humic-like components (Figure 3), which agrees with the involvement of
334 hydroquinones in the autocatalysis of the Fenton reaction (Chen & Pignatello, 1997;
335 Duesterberg & Waite, 2007). The hydroxylation of aromatic moieties into hydroquinones by
336 $^{\bullet}OH$ can explain the increase in fluorescence and no change in absorption in the first 26 h
337 (Figure 1a and 3), because hydroquinone-moieties have high fluorescence and absorption
338 (Cory et al., 2005). Additionally, the breakdown of DOM by $^{\bullet}OH$ decreases the molecular
339 size of DOM and increases the spectral slope coefficient (Figure 1b), which are both related
340 to an increase in the quantum yield of fluorescence (Boyle et al., 2009; Ghigo et al., 2020;
341 Senesi, 1990). The complexation of Fe quenches fluorescence of DOM (Cabaniss, 1992; Du
342 et al., 2018; Poulin et al., 2014; Pullin et al., 2007; Figure 3), because Fe promotes internal
343 conversion and intersystem crossing of the first excited singlet state as well as a ligand to
344 metal charge transfer, i.e., processes that compete with fluorescence (Senesi, 1990). The
345 reduction in fluorescence in the "Fe + KO_2" treatment (Figure 3) is, instead, attributed to the

breakdown of DOM by the extensive amount of $^{\bullet}OH$, suggesting that there is an optimum in fluorescence emission as a function of DOM molecular weight or aromaticity.

5 Conclusions

This study shows that $O_2^{\bullet-}$ can induce the production of $^{\bullet}OH$ in the presence of complexes between Fe and humic DOM. The production of $^{\bullet}OH$ can exceed the stoichiometry of Fenton reaction by 2–24 folds. The autocatalysis of Fenton reaction observed in the present study emphasizes the role of $O_2^{\bullet-}$ as an efficient transformer of organic matter. As numerous processes (photochemistry, abiotic dark oxidation, and biology) can produce $O_2^{\bullet-}$, superoxide-driven Fenton reactions likely transform natural organic matter and contaminants in diverse terrestrial and freshwater environments.

Author Contributions

Y.X., L.C., and A.V.V. all contributed to the preparation, writing, and editing the manuscript. Y.X. and M.-T.N. contributed to the sample collection and measurements. All authors reviewed the manuscript.

Declaration of competing interest

The authors declare no competing financial interest.

Acknowledgements

This study was financially supported by the Academy of Finland Grant (No. 295709) and Taishan Scholar Foundation of Shandong Province (No. tsqn201909126). The stay of L.C. in Jyväskylä was financially supported by the Erasmus+ Traineeship programme. L.C.

acknowledges Compagnia di San Paolo (Torino, Italy) for financially supporting his Ph.D. fellowship.

Appendix A. Supplementary data

Supplementary data to this article can be found online at ***.

References

Aarnos, H., Gélinas, Y., Kasurinen, V., Gu, Y., Puupponen, V.-M., & Vähätalo, A. V. (2018). Photochemical mineralization of terrigenous DOC to dissolved inorganic carbon in ocean. *Global Biogeochemical Cycles*, *32*(2), 250–266. https://doi.org/10.1002/2017GB005698

Aeschbacher, M., Schwarzenbach, R. P., & Sander, M. (2010). Novel electrochemical approach to quantify the redox state of humic substances: Advantages and applications. *Envrionmental Science &Technology*, *44*(1), 87–93.

Arnosti, C. (2004). Speed bumps and barricades in the carbon cycle: Substrate structural effects on carbon cycling. *Marine Chemistry*, *92*, 263–273. https://doi.org/10.1016/j.marchem.2004.06.030

Bhattacharyya, A., Schmidt, M. P., Stavitski, E., Azimzadeh, B., & Martínez, C. E. (2019). Ligands representing important functional groups of natural organic matter facilitate Fe redox transformations and resulting binding environments. *Geochimica et Cosmochimica Acta*, *251*, 157–175. https://doi.org/10.1016/J.GCA.2019.02.027

Boyle, E. S., Guerriero, N., Thiallet, A., Vecchio, R. Del, & Blough, N. V. (2009). Optical Properties of Humic Substances and CDOM: Relation to Structure. *Environmental Science & Technology*, *43*(7), 2262–2268. https://doi.org/10.1021/es803264g

Burgos Castillo, R. C., Fontmorin, J. M., Tang Walter, Z., Xochitl, D. B., & Mika, S. (2018).

Towards reliable quantification of hydroxyl radicals in the Fenton reaction using chemical probes. *RSC Advances*, *8*(10), 5321–5330. https://doi.org/10.1039/c7ra13209c

Cabaniss, S. E. (1992). Synchronous fluorescence-spectra of metal-fulvic acid complexes. *Environmental Science & Technology*, *26*(6), 1133–1139.

Chen, R., & Pignatello, J. J. (1997). Role of quinone intermediates as electron shuttles in Fenton and photoassisted Fenton oxidations of aromatic compounds. *Envrionmental Science &Technology*, *31*, 2399–2406. https://doi.org/10.1021/ES9610646

Cooper, W. J., & Zika, R. G. (1983). Photochemical formation of hydrogen peroxide in surface and ground waters exposed to sunlight. *Science*, *220*(4598), 711–712. https://doi.org/10.1126/science.220.4598.711

Cory, R. M., McKnight, D. M., And, R. M. C., & McKnight, D. M. (2005). Fluorescence spectroscopy reveals ubiquitous presence of oxidized and reduced quinones in dissolved organic matter. *Environmental Science & Technology*, *39*(21), 8142–8149. https://doi.org/10.1021/ES0506962

Diaz, J. M., Hansel, C. M., Voelker, B. M., Mendes, C. M., Andeer, P. F., & Zhang, T. (2013). Widespread production of extracellular superoxide by heterotrophic bacteria. *Science*, *340*(6137), 1223–1226. https://doi.org/10.1126/science.1237331

Diaz, Julia M., & Plummer, S. (2018). Production of extracellular reactive oxygen species by phytoplankton: past and future directions. *Journal of Plankton Research*, *40*, 655–666. https://doi.org/10.1093/plankt/fby039

Dittmar, T., Koch, B., Hertkorn, N., & Kattner, G. (2008). A simple and efficient method for the solid-phase extraction of dissolved organic matter (SPE-DOM) from seawater. *Limnology and Oceanography: Methods*, *6*(6), 230–235. https://doi.org/10.4319/lom.2008.6.230

Du, Y., Ramirez, C. E., & Jaffé, R. (2018). Fractionation of dissolved organic matter by co-

precipitation with iron: Effects of composition. *Environmental Processes*, *5*(1), 5–21. https://doi.org/10.1007/s40710-017-0281-4

Duesterberg, C. K., & Waite, T. D. (2007). Kinetic modeling of the oxidation of p - hydroxybenzoic acid by Fenton's reagent: Implications of the role of quinones in the Redox cycling of iron. *Environmental Science & Technology*, *41*(11), 4103–4110. https://doi.org/10.1021/es0628699

Einola, E., Rantakari, M., Kankaala, P., Kortelainen, P., Ojala, A., Pajunen, H., et al. (2011). Carbon pools and fluxes in a chain of five boreal lakes: A dry and wet year comparison. *Journal of Geophysical Research: Biogeosciences*, *116*, G03009. https://doi.org/10.1029/2010JG001636

Fujii, M., & Otani, E. (2017). Photochemical generation and decay kinetics of superoxide and hydrogen peroxide in the presence of standard humic and fulvic acids. *Water Research*, *123*, 642–654. https://doi.org/10.1016/j.watres.2017.07.015

Fujii, M., Imaoka, A., Yoshimura, C., & Waite, T. D. (2014). Effects of molecular composition of natural organic matter on ferric iron complexation at circumneutral pH. *Environmental Science & Technology*, *48*(8), 4414–4424. https://doi.org/10.1021/es405496b

Gao, H., & Zepp, R. G. (1998). Factors influencing photoreactions of dissolved organic matter in a coastal river of the southeastern United States. *Envrionmental Science &Technology*, *32*, 2940–2946.

Garg, S., Rose, A. L., & Waite, T. D. (2011). Photochemical production of superoxide and hydrogen peroxide from natural organic matter. *Geochimica et Cosmochimica Acta*, *75*(15), 4310–4320. https://doi.org/10.1016/j.gca.2011.05.014

Garg, S., Jiang, C., & Waite, T. D. (2018). Impact of pH on iron redox transformations in simulated freshwaters containing natural organic matter. *Environmental Science &*

Technology, *52*(22), 13184–13194. https://doi.org/10.1021/acs.est.8b03855

Georgi, A., Schierz, A., Trommler, U., Horwitz, C. P., Collins, T. J., & Kopinke, F. D. (2007). Humic acid modified Fenton reagent for enhancement of the working pH range. *Applied Catalysis B: Environmental*, *72*(1–2), 26–36. https://doi.org/10.1016/j.apcatb.2006.10.009

Ghigo, G., Vione, D., & Berto, S. (2020). Experimental and theoretical study of the fluorescence emission of ferulic acid: Possible insights into the fluorescence properties of humic substances. *Spectrochimica Acta - Part A: Molecular and Biomolecular Spectroscopy*, *228*, 117587. https://doi.org/10.1016/j.saa.2019.117587

Gil-Lozano, C., Davila, A. F., Losa-Adams, E., Fairén, A. G., & Gago-Duport, L. (2017). Quantifying Fenton reaction pathways driven by self-generated H_2O_2 on pyrite surfaces. *Scientific Reports*, *7*, 43703. https://doi.org/10.1038/srep43703

Goldstone, J. V., Pullin, M. J., Bertilsson, S., Voelker, B. M., & Hole, W. (2002). Reactions of hydroxyl radical with humic substances : Bleaching , mineralization , and production of bioavailable carbon substrates. *Environmental Science & Technology*, *36*(3), 364–372. https://doi.org/10.1021/ES0109646

Goldstone, Jared V., & Voelker, B. M. (2000). Chemistry of superoxide radical in seawater: CDOM associated sink of superoxide in coastal waters. *Environmental Science & Technology*, *34*(6), 1043–1048. https://doi.org/10.1021/es9905445

Hayyan, M., Hashim, M. A., & AlNashef, I. M. (2016). Superoxide ion: Generation and chemical implications. *Chemical Reviews*, *116*(5), 3029–3085. https://doi.org/10.1021/acs.chemrev.5b00407

Helms, J. R., Stubbins, A., Ritchie, J. D., Minor, E. C., Kieber, D. J., & Mopper, K. (2008). Absorption spectral slopes and slope ratios as indicators of molecular weight, source, and photobleaching of chromophoric dissolved organic matter. *Limnology and*

Oceanography, *53*(3), 955–969. https://doi.org/10.4319/lo.2008.53.3.0955

Hongve, D., Riise, G., & Kristiansen, J. F. (2004). Increased colour and organic acid concentrations in Norwegian forest lakes and drinking water - A result of increased precipitation? *Aquatic Sciences*, *66*(2), 231–238. https://doi.org/10.1007/s00027-004-0708-7

Imlay, J. A. (2004). Pathways of oxidative damage. *Annual Review of Microbiology*, *57*(1), 395–418. https://doi.org/10.1146/annurev.micro.57.030502.090938

Karlsson, T., & Persson, P. (2012). Complexes with aquatic organic matter suppress hydrolysis and precipitation of Fe(III). *Chemical Geology*, *322–323*, 19–27. https://doi.org/10.1016/j.chemgeo.2012.06.003

Koehler, B., Landelius, T., Weyhenmeyer, G. A., Machida, N., & Tranvik, L. J. (2014). Sunlight-induced carbon dioxide emissions from inland waters. *Global Biogeochemical Cycles*, *28*(7), 696–711. https://doi.org/10.1002/2014GB004850

Kothawala, D., Kellerman, A., Catalan, N., & Tranvik, L. (2016). Controls on the dynamics of dissolved organic matter in boreal lakes. *Geophysical Research Abstracts EGU General Assembly*, *18*(April), 13894. https://doi.org/10.1097/00010694-200004000-00001

Lee, S., Roh, Y., & Koh, D.-C. (2019). Oxidation and reduction of redox-sensitive elements in the presence of humic substances in subsurface environments: A review. *Chemosphere*, *220*, 86–97. https://doi.org/10.1016/j.chemosphere.2018.11.143

Liao, P., Yu, K., Lu, Y., Wang, P., Liang, Y., & Shi, Z. (2019). Extensive dark production of hydroxyl radicals from oxygenation of polluted river sediments. *Chemical Engineering Journal*, *368*, 700–709. https://doi.org/10.1016/j.cej.2019.03.018

Louit, G., Foley, S., Cabillic, J., Coffigny, H., Taran, F., Valleix, A., et al. (2005). The reaction of coumarin with the OH radical revisited: Hydroxylation product analysis

determined by fluorescence and chromatography. *Radiation Physics and Chemistry*, *72*(2–3), 119–124. https://doi.org/10.1016/j.radphyschem.2004.09.007

Ma, J., Del Vecchio, R., Golanoski, K. S., Boyle, E. S., & Blough, N. V. (2010). Optical properties of humic substances and CDOM: Effects of borohydride reduction. *Environmental Science & Technology*, *44*(14), 5395–5402. https://doi.org/10.1021/es100880q

Micinski, E., Ball, L. A., & Zafiriou, O. C. (1993). Photochemical oxygen activation: Superoxide radical detection and production rates in the eastern Caribbean. *Journal of Geophysical Research: Oceans*, *98*(C2), 2299–2306. https://doi.org/10.1029/92JC02766@10.1002/(ISSN)2169-9291.PECW1

Minella, M., De Laurentiis, E., Maurino, V., Minero, C., & Vione, D. (2015). Dark production of hydroxyl radicals by aeration of anoxic lake water. *Science of the Total Environment*, *527–528*, 322–327. https://doi.org/10.1016/j.scitotenv.2015.04.123

Mostovaya, A., Hawkes, J. A., Dittmar, T., & Tranvik, L. J. (2017). Molecular determinants of dissolved organic matter reactivity in lake water. *Frontiers in Earth Science*, *5*, 106. https://doi.org/10.3389/feart.2017.00106

Murphy, K. R., Stedmon, C. A., Graeber, D., & Bro, R. (2013). Fluorescence spectroscopy and multi-way techniques. PARAFAC. *Analytical Methods*, *5*(23), 6557. https://doi.org/10.1039/c3ay41160e

Neubauer, E., Köhler, S. J., von der Kammer, F., Laudon, H., Hofmann, T., Neubauer, E., et al. (2013). Effect of pH and stream order on iron and arsenic speciation in boreal catchments. *Environmental Science & Technology*, *47*(13), 1–14. https://doi.org/10.1021/es401193j

Page, S. E., Sander, M., Arnold, W. A., & McNeill, K. (2012). Hydroxyl radical formation upon oxidation of reduced humic acids by oxygen in the dark. *Environmental Science &*

Technology, *46*(3), 1590–1597. https://doi.org/10.1021/es203836f

Page, S. E., Kling, G. W., Sander, M., Harrold, K. H., Logan, J. R., McNeill, K., & Cory, R. M. (2013). Dark formation of hydroxyl radical in arctic soil and surface waters. *Environmental Science & Technology*, *47*(22), 12860–12867. https://doi.org/10.1021/es4033265

Page, S. E., Logan, J. R., Cory, R. M., & McNeill, K. (2014). Evidence for dissolved organic matter as the primary source and sink of photochemically produced hydroxyl radical in arctic surface waters. *Environmental Sciences: Processes and Impacts*, *16*(4), 807–822. https://doi.org/10.1039/c3em00596h

Piccolo, A. (1996). *Humic substances in terrestrial ecosystems*. (A. Piccolo, Ed.). Amsterdam: Elsevier Science.

Pignatello, J. J., Oliveros, E., & MacKay, A. (2006). Advanced oxidation processes for organic contaminant destruction based on the fenton reaction and related chemistry. *Critical Reviews in Environmental Science and Technology*, *36*(1), 1–84. https://doi.org/10.1080/10643380500326564

Poulin, B. A., Ryan, J. N., & Aiken, G. R. (2014). The effects of iron on optical properties of dissolved organic matter. *Environmental Science & Technology*, *48*(17), 10098–10106. https://doi.org/10.1021/es502670r

Pullin, M. J., Anthony, C., & Maurice, P. A. (2007). Effects of iron on the molecular weight distribution, light absorption, and fluorescence properties of natural organic matter. *Environmental Engineering Science*, *24*(8), 987–997. https://doi.org/10.1089/ees.2006.0040

Rose, A. L., & Waite, T. D. (2005). Reduction of organically complexed ferric iron by superoxide in a simulated natural water. *Environmental Science & Technology*, *39*(February), 2645–2650. https://doi.org/10.1021/es048765k

Rush, J. D., & Bielski, B. H. J. (2005). Pulse radiolytic studies of the reaction of perhydroxyl/superoxide O_2^- with iron(II)/iron(III) ions. The reactivity of HO_2/O_2^- with ferric ions and its implication on the occurrence of the Haber-Weiss reaction. *The Journal of Physical Chemistry*, *89*(23), 5062–5066. https://doi.org/10.1021/j100269a035

Senesi, N. (1990). Molecular and quantitative aspects of the chemistry of fulvic acid and its interactions with metal ions and organic chemicals. *Analytica Chimica Acta*, *232*, 77–106. https://doi.org/10.1016/S0003-2670(00)81226-X

Southworth, B. A., & Voelker, B. M. (2003). Hydroxyl radical production via the photo-Fenton reaction in the presence of fulvic acid. *Environmental Science & Technology*, *37*(6), 1130–1136. https://doi.org/10.1021/es020757l

Tranvik, L. J. (1988). Availability of dissolved organic carbon for planktonic bacteria in oligotrophic lakes of differing humic content. *Microbial Ecology*, *16*(3), 311–322. https://doi.org/10.1007/BF02011702

Trusiak, A., Treibergs, L. A., Kling, G. W., & Cory, R. M. (2018). The role of iron and reactive oxygen species in the production of CO_2 in arctic soil waters. *Geochimica et Cosmochimica Acta*, *224*, 80–95. https://doi.org/10.1016/j.gca.2017.12.022

Vähätalo, A. V., Salonen, K., Münster, U., Järvinen, M., & Wetzel, R. G. (2003). Photochemical transformation of allochthonous organic matter provides bioavailable nutrients in a humic lake. *Archiv Fur Hydrobiologie*, *156*(3), 287–314. https://doi.org/10.1127/0003-9136/2003/0156-0287

Voelker, B. M., & Sulzberger, B. (1996). Effects of fulvic acid on Fe(II) oxidation by hydrogen peroxide. *Environmental Science & Technology*, *30*(4), 1106–1114. https://doi.org/10.1021/es9502132

Voelker, B. M., Morel, F. M. M., & Sulzberger, B. (1997). Iron redox cycling in surface waters: Effects of humic substances and light. *Environmental Science & Technology*,

570 *31*(4), 1004–1011. https://doi.org/10.1021/es9604018

571 Vogt, R. D., Akkanen, J., Andersen, D. O., Brüggemann, R., Chatterjee, B., Gjessing, E., et al.
572 (2004). Key site variables governing the functional characteristics of Dissolved Natural
573 Organic Matter (DNOM) in Nordic forested catchments. *Aquatic Sciences - Research*
574 *Across Boundaries*, *66*(2), 195–210. https://doi.org/10.1007/s00027-004-0710-0

575 Waggoner, D. C., Wozniak, A. S., Cory, R. M., & Hatcher, P. G. (2017). The role of reactive
576 oxygen species in the degradation of lignin derived dissolved organic matter.
577 *Geochimica et Cosmochimica Acta*, *208*, 171–184.
578 https://doi.org/10.1016/j.gca.2017.03.036

579 Wu, Y., Zhou, S., Qin, F., Peng, H., Lai, Y., & Lin, Y. (2010). Removal of humic substances
580 from landfill leachate by Fenton oxidation and coagulation. *Process Safety and*
581 *Environmental Protection*, *88*(4), 276–284. https://doi.org/10.1016/j.psep.2010.03.002

582 Yuan, X., Davis, J. A., & Nico, P. S. (2016). Iron-mediated oxidation of
583 Methoxyhydroquinone under dark conditions: Kinetic and mechanistic insights.
584 *Environmental Science & Technology*, *50*(4), 1731–1740.
585 https://doi.org/10.1021/acs.est.5b03939

586 Yurkova, I. L., Schuchmann, H. P., & Von Sonntag, C. (1999). Production of OH radicals in
587 the autoxidation of the Fe(II)-EDTA system. *Journal of the Chemical Society. Perkin*
588 *Transactions 2*, (10), 2049–2052. https://doi.org/10.1039/a904739e

589 Zhang, P., & Yuan, S. (2017). Production of hydroxyl radicals from abiotic oxidation of
590 pyrite by oxygen under circumneutral conditions in the presence of low-molecular-
591 weight organic acids. *Geochimica et Cosmochimica Acta*, *218*, 153–166.
592 https://doi.org/10.1016/j.gca.2017.08.032

593 Zhang, T., Hansel, C. M., Voelker, B. M., & Lamborg, C. H. (2016). Extensive dark
594 biological production of reactive oxygen species in brackish and freshwater ponds.

595 *Environmental Science & Technology*, *50*(6), 2983–2993.
596 https://doi.org/10.1021/acs.est.5b03906
597 Zhang, Yi, & Blough, N. V. (2016). Photoproduction of one-electron reducing intermediates
598 by chromophoric dissolved organic matter (CDOM): Relation to O_2^- and H_2O_2
599 photoproduction and CDOM photooxidation. *Environmental Science & Technology*,
600 *50*(20), 11008–11015. https://doi.org/10.1021/acs.est.6b02919
601 Zhang, Ying, & Zhou, M. (2019). A critical review of the application of chelating agents to
602 enable Fenton and Fenton-like reactions at high pH values. *Journal of Hazardous*
603 *Materials*, *362*, 436–450. https://doi.org/10.1016/j.jhazmat.2018.09.035
604

605 **Tables**

606 **Table 1.** Experimental design. The initial concentrations of DOM, complexed Fe, KO_2, and
607 coumarin in the treatments made in artificial lake water (Table S1).

Treatments	DOM (mg L^{-1})	Fe (µM)	KO_2 (µM)	Coumarin (µM)
control	20	0.17*	--	10
KO_2***	20	0.17*	13	10
Fe	20	20**	--	10
Fe + KO_2***	20	20**	13	10

608 --, no addition of KO_2. *residual Fe in extracted DOM (8.5 nmol Fe/mg DOM), **introduced
609 as DOM-Fe complex. ***In the treatments "KO_2" and "Fe + KO_2", the introduction of 13 µM
610 KO_2 increased pH to 12.2, which was soon titrated with HCl back to the same pH 5 as in the
611 other treatments.
612

613 **Table 2.** Cumulative production of $^{\bullet}OH$ radicals (μM) in the treatments.
614

Time Interval	control	Fe	KO_2	Fe + KO_2
0–10 h	0.09	0.11	1.32	16.3
0–168 h	0.23	0.57	9.88	103.5

615

Figure captions

Figure 1. Absorption coefficient of CDOM at 410 nm (a_{410}) and spectral slope coefficient ($S_{275\text{-}295}$) after 26 h and 168 h incubations in the three treatments and the control. Table 1 explains the treatments. Stars indicate a significant difference between the treatments and the control, * $P < 0.05$ and ** $P < 0.01$. Error bars show standard deviations of three replicated treatments.

Figure 2. Overlaid spectra of four components (PARAFAC model). The figure shows six unique splits vs. the overall model. Dot lines indicate excitation spectra and solid lines indicate emission spectra. The excitation and emission maxima of each components are shown in Table S2. The loadings in the Y-axis indicate the normalized component intensity in the PARAFAC modeling.

Figure 3. Fluorescent intensities at 168 h of four components obtained from EEM-PARAFAC modeling (Figure 2). The fluorescence of component 4 was negligible in the "Fe+KO_2" treatment. Stars indicate a significant difference between treatment and the control, * $P < 0.05$ and ** $P < 0.01$. Error bars show standard deviations of three replicated treatments.

Figure 4. Computed formation rate of $^{\bullet}$OH in the treatments at selected times (■). The blue lines represent the fitting functions from which the cumulative production of $^{\bullet}$OH radicals were calculated. The R^2 parameter shows the goodness of the fit. See SI for the fitting functions. Note the orders of magnitude differences in the scales of Y-axes.

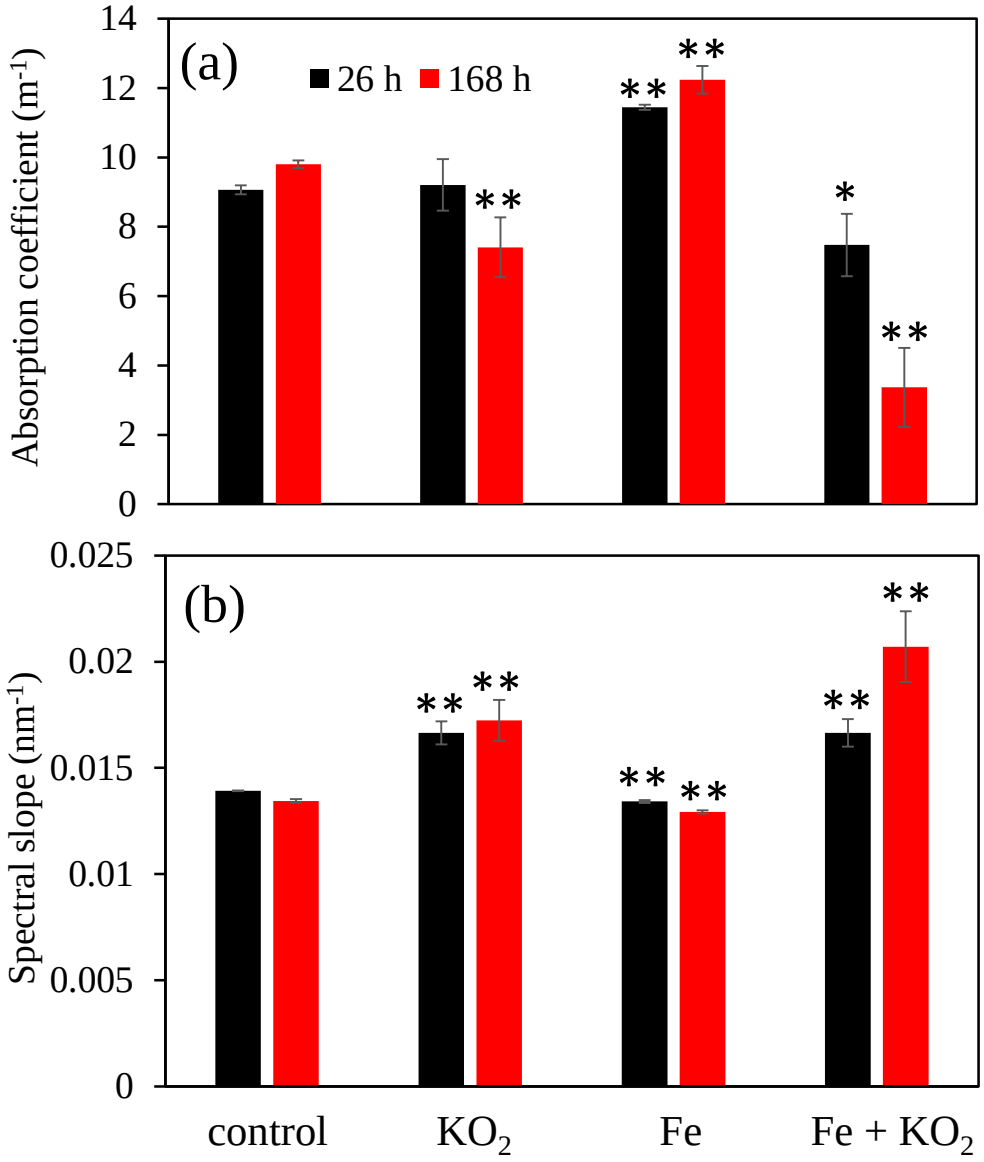

Figure 1. Absorption coefficient of CDOM at 410 nm (a_{410}) and spectral slope coefficient ($S_{275\text{-}295}$) after 26 h and 168 h incubations in the three treatments and the control. Table 1 explains the treatments. Stars indicate a significant difference between the treatments and the control, * $P < 0.05$ and ** $P < 0.01$. Error bars show standard deviations of three replicated treatments.

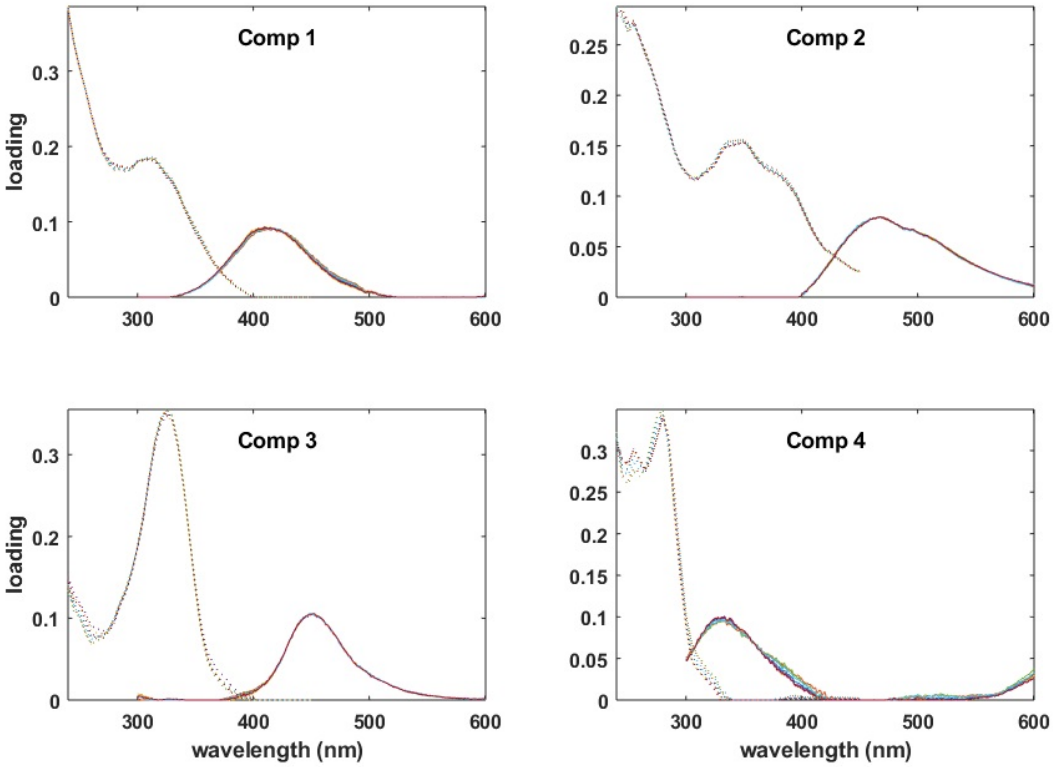

Figure 2. Overlaid spectra of four components (PARAFAC model). The figure shows six unique splits vs. the overall model. Dot lines indicate excitation spectra and solid lines indicate emission spectra. The excitation and emission maxima of each components are shown in Table S2. The loadings in the Y-axis indicate the normalized component intensity in the PARAFAC modeling.

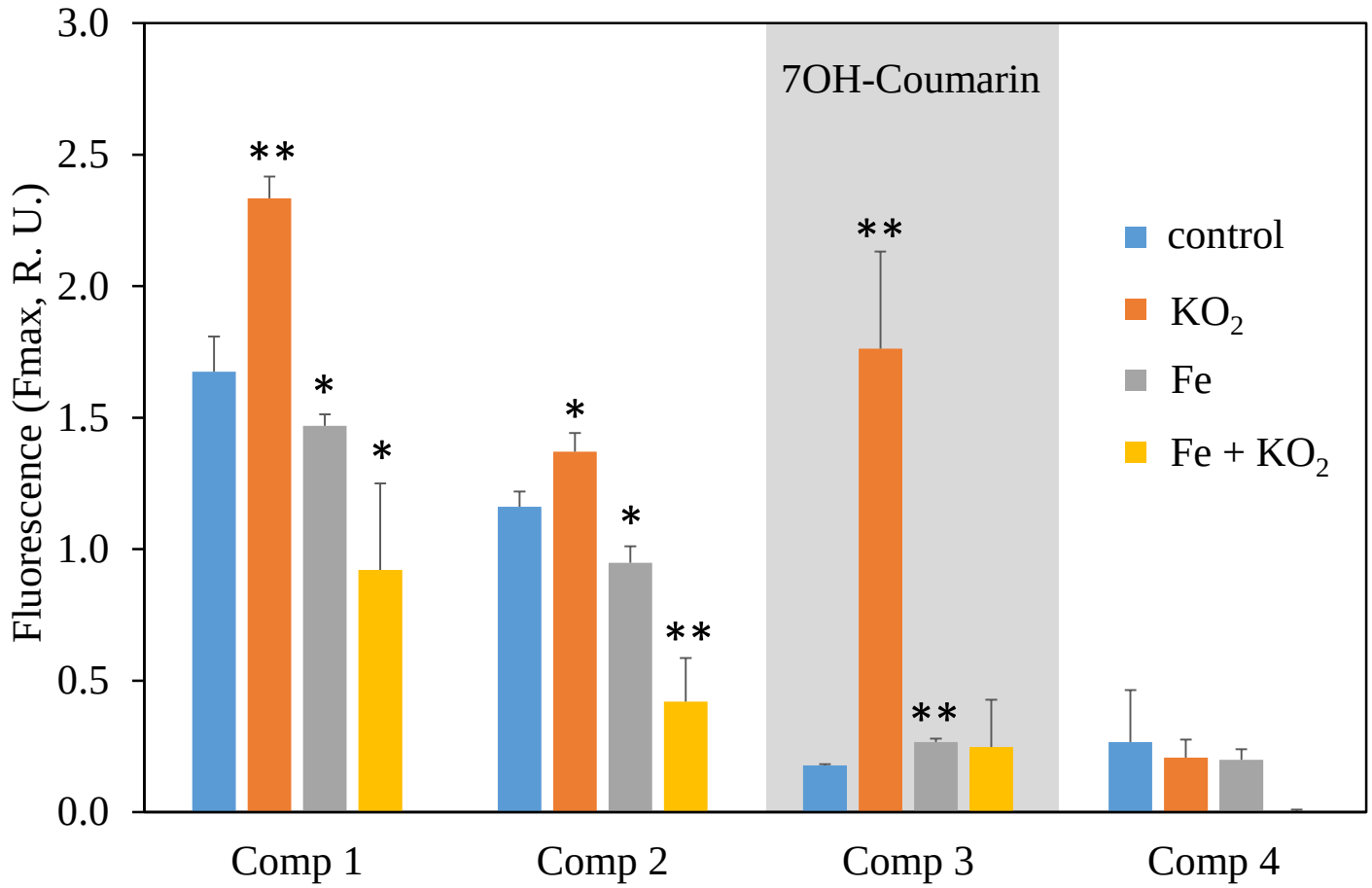

Figure 3. Fluorescent intensities at 168 h of four components obtained from EEM-PARAFAC modeling (Figure 2). The fluorescence of component 4 was negligible in the "Fe+KO_2" treatment. Stars indicate a significant difference between treatment and the control, * $P < 0.05$ and ** $P < 0.01$. Error bars show standard deviations of three replicated treatments.

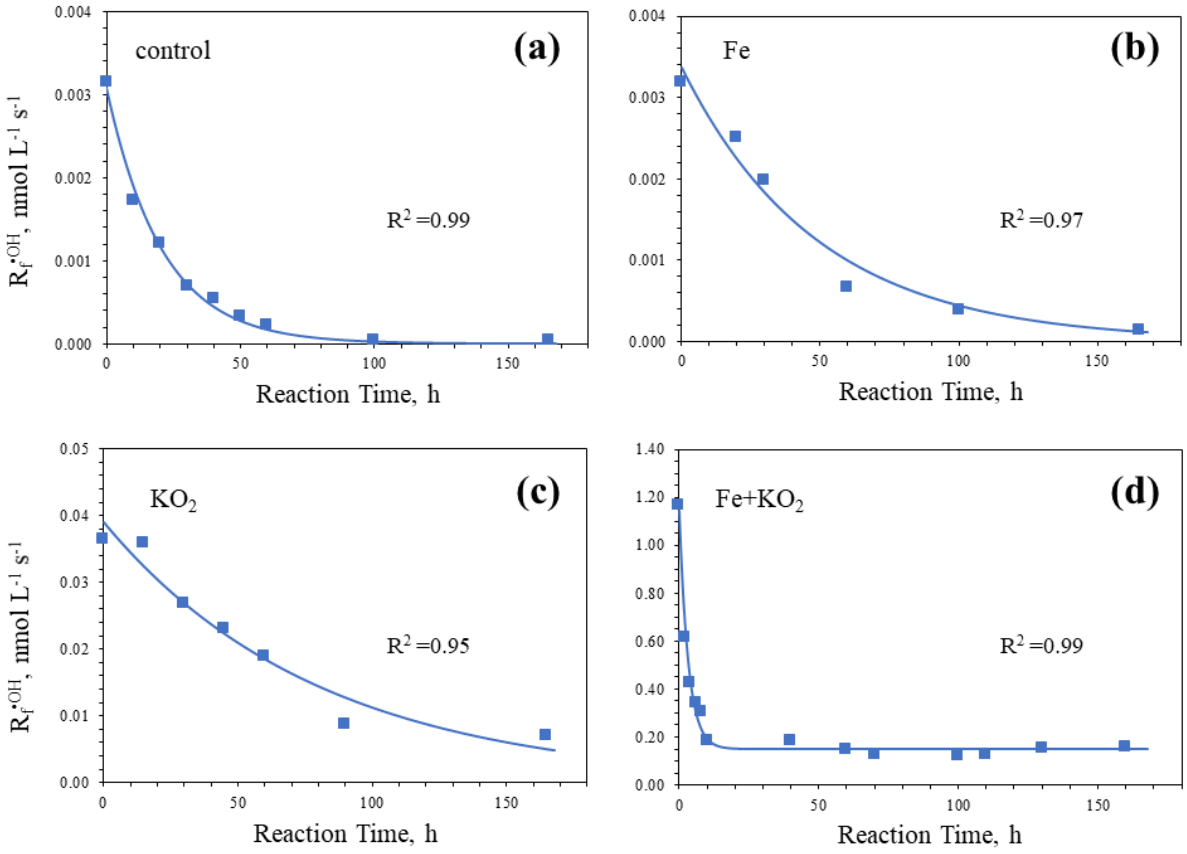

Figure 4. Computed formation rate of $^{\bullet}$OH in the treatments at selected times (■). The blue lines represent the fitting functions from which the cumulative production of $^{\bullet}$OH radicals were calculated. The R^2 parameter shows the goodness of the fit. See SI for the fitting functions. Note the orders of magnitude differences in the scales of Y-axes.

Highlights

- $O_2^{\bullet-}$ can induce the production of $^{\bullet}OH$ in the presence of DOM and Fe complexes
- The production of $^{\bullet}OH$ exceeds the stoichiometry of Fenton reaction by 2–24 folds
- $^{\bullet}OH$ produced from $O_2^{\bullet-}$ extensively modified the spectroscopic properties of DOM
- $O_2^{\bullet-}$ can trigger an autocatalytic Fenton reaction and produce $^{\bullet}OH$ to break down DOM
- $O_2^{\bullet-}$ driven Fenton reaction may explain DOM transformation in multiple environment

Supplementary Information

Superoxide-driven autocatalytic dark production of hydroxyl radicals in the presence of complexes of natural dissolved organic matter and iron

Yihua Xiao[1,2*], Luca Carena[3], Marja-Terttu Näsi[1], Anssi V. Vähätalo[1]

[1]Department of Biological and Environmental Science, University of Jyväskylä, 40014 Jyväskylä, Finland

[2]School of Environmental & Municipal Engineering, Qingdao University of Technology, 266033 Qingdao, China

[3]Dipartimento di Chimica, Università di Torino, Via Pietro Giuria 5, 10125 Torino, Italy

This Supplementary Information contains:

Table S1. Composition of artificial lake water. The concentrations refer to the final concentrations in the beginning of the experiment.

	Final concentration ($\mu mol\ L^{-1}$)
Na_2SO_4	54
KCl	7.9
$MgCl_2 \cdot 2H_2O$	28.8
$CaCl_2 \cdot 2H_2O$	60
$MnSO_4 \cdot H_2O$	0.31
$NaHCO_3$	0.04
$Na_2SiO_3 \cdot 5H_2O$	82
$NaNO_3$	5.0
NH_4Cl	0.03
$C_3H_{17}Na_2O_6P \cdot 6H_2O$*	21

*β-glycerophosphate disodium salt hydrate

Table S2. Description of four fluorescence components identified by PARAFAC

Component	Excitation/Emission maxima (nm)	Description
Comp 1	240(310)/415	Humic-like material with low molecular weight and aromaticity, common in marine environment but is also widely found in (boreal) freshwater, originated from biological activity (Coble et al., 1998; Gu et al., 2018; Kothawala et al., 2014; Zhang et al., 2009)
Comp 2	240(350)/459	Terrestrially-derived humic-like material with high molecular weight and aromaticity, is widely found but highest in forested environments and wetlands (Coble et al., 1990; Kothawala et al., 2014; Parlanti et al., 2000)
Comp 3	325/453	7OH-coumarin (Louit et al., 2005)
Comp 4	280/333	Tryptophan-like amino acid, free or bound on proteins indicating more degraded materials (Cory et al., 2005; Kothawala et al., 2014; Stedmon et al., 2003)

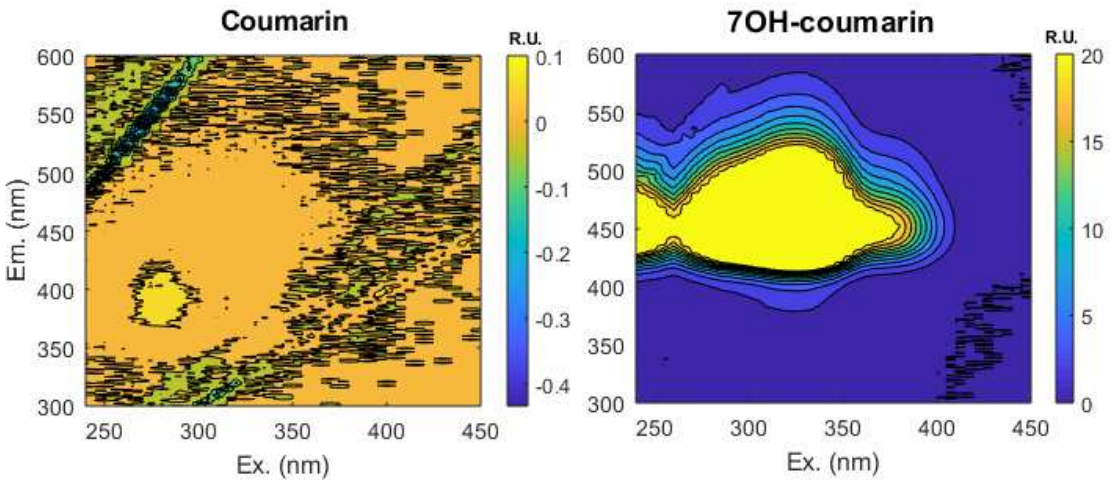

Figure S1. Excitation emission matrices for coumarin (left, 10 µmol L^{-1}) and 7OH-coumarin (right, 10 µmol L^{-1}). Note that the fluorescence of coumarin (given in units relative to the Raman of H_2O; R.U.) is nearly negligible

Text SI: Calculations on the $O_2^{\bullet-}$ disproportionation and DOM-Fe(III) reduction by $O_2^{\bullet-}$ in treatment of "Fe + KO_2"

This section will evaluate the reactions of superoxide ($O_2^{\bullet-}$) in the beginning of treatment "Fe + KO_2" containing 20 µmol L^{-1} DOM-Fe(III) and artificial lake water (Table S1). The Scheme SI-1 shows that $O_2^{\bullet-}$ can be either reduced to H_2O_2 or oxidized to O_2 (Fujii & Otani, 2017). Disproportionation can convert $O_2^{\bullet-}$ to H_2O_2 either spontaneously or though the catalysis by reduced metals or DOM, marked collectively as X_{red} in Scheme SI-1. Alternatively, oxidized DOM or metals (X_{ox}) can oxidize $O_2^{\bullet-}$ to O_2 (Scheme SI-I).

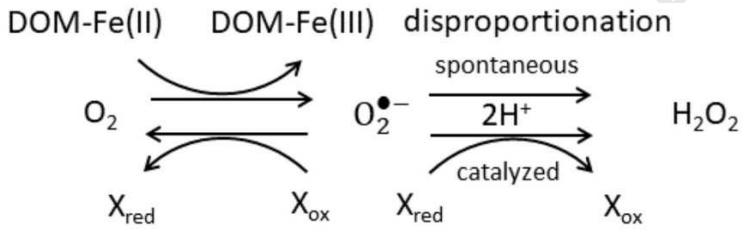

Scheme SI-1. Possible fates of superoxide in the treatment "Fe + KO_2" (modified from Fujii & Otani, 2017). X_{red} and X_{ox} refer to reduced and oxidized forms of metals or DOM.

In this study, the hydroxyl radical ($^{\bullet}OH$) production was an order of magnitude higher in the "KO_2 + Fe" treatment with DOM-Fe(III) than in the "KO_2" treatment with DOM alone. This finding suggests that the reaction of $O_2^{\bullet-}$ with DOM-Fe(III) (from X_{ox} to X_{red} in Scheme SI-1) played a major role in the production of $^{\bullet}OH$. Artificial lake water contained 0.31 µmol L^{-1} Mn(II) (i.e., X_{red} in Scheme SI-1), which can catalyze disproportionation of $O_2^{\bullet-}$ to H_2O_2 in addition to bimolecular disproportionation. One should notice that disproportionation requires also H^+ (Scheme SI-1), and thus the process is sensitive to pH. In this study, the introduction of KO_2 in 0.05 mol L^{-1} NaOH solution resulted in 13 µmol L^{-1} $O_2^{\bullet-}$ concentration but at the same time increased the pH of artificial lake water to 12.2. The calculations below indicate that at pH 12.2 the rate of disproportionation was negligible sink compared to DOM-Fe(III).

(1) Disproportionation of superoxide and hydroperoxy radical

The conjugate acid of $O_2^{\bullet-}$, hydroperoxy radical ($HO_2^{\bullet}$) forms when a superoxide anion ($O_2^{\bullet-}$) accepts a hydrogen ion:

$HO_2^{\bullet} \rightleftarrows O_2^{\bullet-} + H^+$ (Eq. SI-1).

For the equation of 1:

$K_{HO2} = [O_2^{\bullet-}]\,[H^+]/[HO_2^{\bullet}]$,

the equilibrium constant, K_{HO2}, is 1.6×10^{-5} L mol^{-1} (Bielski et al., 1985).

Spontaneous disproportionation of $HO_2^{\bullet}$ and $O_2^{\bullet-}$ to H_2O_2 and molecular O_2 can proceed either through:

$HO_2^{\bullet} + HO_2^{\bullet} \rightarrow H_2O_2 + O_2$ (Eq. SI-2)

with a second order rate constant, $k_2 = 8.3 \times 10^5$ L mol^{-1} s^{-1} (Bielski et al. 1985) or through:

$HO_2^{\bullet} + O_2^{\bullet-} + H_2O \rightarrow H_2O_2 + O_2 + OH^-$ (Eq. SI-3)

with a second order rate constant, $k_3 = 9.7 \times 10^7$ L mol^{-1} s^{-1} (Bielski et al., 1985).

Because $HO_2^{\bullet}$ is in an equilibrium with $O_2^{\bullet-}$ (Eq. SI-1), it is convenient to examine their concentrations together: $O_2^* = HO_2^{\bullet} + O_2^{\bullet-}$. In this case, the two separate disproportionation reactions can be presented together as:

$O_2^* + O_2^* + 2H^+ \rightarrow H_2O_2 + O_2$ (Eq. SI-4),

where the second order rate constant, k_4, can be calculated with the combination of k_2 and k_3 accounting for the equilibrium between $O_2^{\bullet-}$ and $HO_2^{\bullet}$ (Eq. SI-1):

$k_4 = (k_2 + k_3 (K_{HO2}/[H^+])) (1 + K_{HO2}/[H^+])^{-2}$ (Bielski et al., 1985).

The formation rate of H_2O_2 or molecular O_2 (mol L^{-1} s^{-1}) through disproportionation is:

$R_{H2O2,O2} = k_4 [O_2^*][O_2^*]$ (Eq. SI-5)

The rate of O_2^* consumption (mol L^{-1} s^{-1}) is:

$R_{O2*} = -2k_4 [O_2^*][O_2^*]$ (Eq. SI-6)

The temporal kinetics of O_2^* concentration (mol L^{-1}) can be described as:

$[O_2^*] = [O_2^*]_0/(1 + 2k_4 [O_2^*]_0 t)$ (Eq. SI-7)

where $[O_2^*]_0$ refers to the initial concentration of O_2^*.

and the half-life of O_2^* (s) is:

$t_{½,O2*} = (2k_4 [O_2^*]_0)^{-1}$ (Eq. SI-8)

At pH 12.2, $k_4 = 3.83$ L mol^{-1} s^{-1} and the half-life of the introduced O_2^* through disproportionation was 10054 s (= 2.79 hours) when calculated according to Eq. SI-8.

Manganese can react with superoxide at fast rate:

$Mn(II) + O_2^{\bullet-} \rightarrow MnO_2^+$ (Eq. SI-9)

and in this study convert 0.31 µmol L^{-1} (or 2.4% of introduced KO_2) into manganous superoxide (Wuttig et al., 2013). In seawater, MnO_2^+ behaves like $O_2^{\bullet-}$ and its major fate is disproportionation (Wuttig et al., 2013). At pH 12.2 of present study, the rate of disproportionation of MnO_2^+ is slow, if it behaves like $O_2^{\bullet-}$ (see above). Instead, MnO_2^+ is expected to form an equilibrium with Mn(II) and $O_2^{\bullet-}$ (Wuttig et al., 2013):

$MnO_2^+ \rightleftarrows Mn(II) + O_2^{\bullet-}$ (Eq. SI-10)

and $O_2^{\bullet-}$ will be eventually consumed by DOM-Fe(III) at pH 12.2 in the beginning of the "KO_2 + Fe" treatment.

(2) Reduction of DOM-Fe(III) by $O_2^{\bullet-}$

The reduction of DOM-Fe(III) by $O_2^{\bullet-}$ can be expressed as,

DOM-Fe(III) + $O_2^{\bullet-} \rightarrow$ DOM-Fe(II) + O_2 (Eq. SI-11a).

The rate of superoxide consumption, DOM-Fe(III) loss and DOM-Fe(II) formation can be calculated as:

$rate = k_{11} [O_2^*] [\text{DOM-Fe(III)}]$ (Eq. SI-11b).

The second-order rate constant for the reaction SI-11 ($k_{11} = 2.8 \times 10^5$ L mol^{-1} s^{-1}) has been determined at pH 8 using Suwannee River fulvic acid (SRFA) as a source of DOM (Garg et al., 2007). Using $k_{11} = 2.8 \times 10^5$ L mol^{-1} s^{-1}, the reaction Eq. SI-11 consumed $O_2^{\bullet-}$ and produced 13 µmol DOM-Fe(II) within about two seconds after the introduction of KO_2.

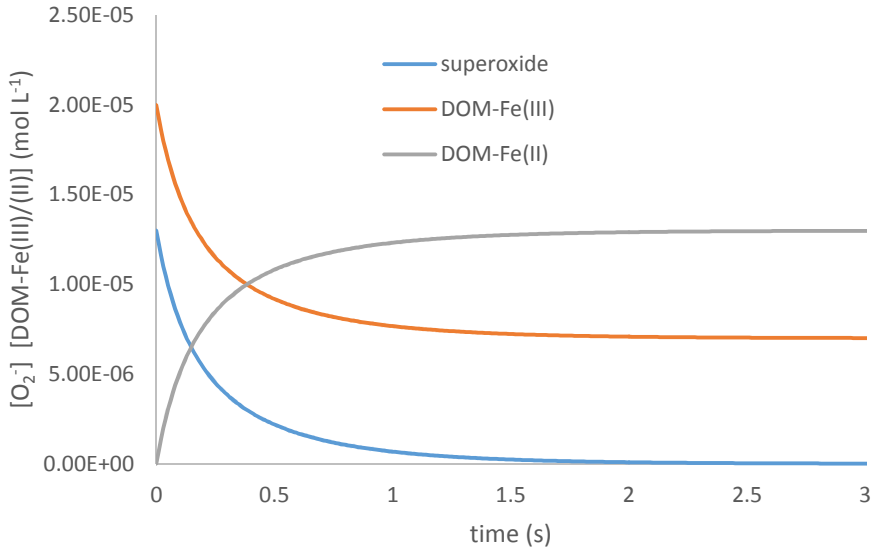

Figure SI-1. Calculated (Eq. SI-11) concentrations of superoxide (O_2^-), DOM-Fe(III) and DOM-Fe(II) in the beginning of "Fe + KO_2" treatment at pH 12.2.

3) The Fenton process in the beginning of experiment after the adjustment of pH to 5

After the introduction of KO_2 and rapid reduction of DOM-Fe(III) by $O_2^{\bullet-}$, the pH of artificial lake water was adjusted to 5. Under those conditions, the concentration of superoxide was initially negligible, but the water contained 13 µmol L^{-1} DOM-Fe(II) (Figure SI-1). The artificial lake water was in contact with atmosphere and contained 264 µmol L^{-1} dissolved O_2 according to the solubility of O_2 to fresh water at +25°C.

The oxidation of DOM-Fe(II) can lead to the production of $^{\bullet}OH$ through the following sequence of reactions.

Dissolved O_2 can oxidize DOM-Fe(II):

$$\text{DOM-Fe(II)} + O_2 \rightarrow \text{DOM-Fe(III)} + O_2^* \qquad \text{(Eq. SI-12)}$$

and produce O_2^* with k_{12} = 100 L mol^{-1} s^{-1} determined for SRFA (Garg et al., 2007). The loss of DOM-Fe(II) through Eq. SI-12 is calculated in Figure SI-2a.

DOM-Fe(II) can also dissociate:

$$\text{DOM-Fe(II)} \rightarrow \text{DOM} + \text{Fe(II)} \qquad \text{(Eq. SI-13)}$$

with $k_{13} = 8 \times 10^{-4}$ s^{-1} (Garg et al., 2007). Immediately after the pH adjustment to 5, the calculated rate of dissociation (1.04×10^{-8} mol L s^{-1}; Eq. SI-13) is an order of magnitude

lower than the oxidation of DOM-Fe(II) by O_2 (3.6×10^{-7} mol L s^{-1}; Eq. SI-12). This indicates that Eq. SI-12 was primarily responsible for the production of O_2^* and for simplicity the dissociation of DOM-Fe(II) is omitted in kinetic modelling presented in Figure SI-2.

At pH 5, the spontaneous disproportionation of O_2^* (Eq. SI-4; $k_4 = 2.3 \times 10^7$ L mol^{-1} s^{-1}) leads to a fast production of H_2O_2 (Figure SI-2a). DOM-Fe(II) reacts faster with H_2O_2 (Eq. SI-14; $k_{14} = 1.75 \times 10^4$ L mol^{-1} s^{-1}) (Pignatello et al., 2006) than with O_2 (Eq. SI-12):

$$\text{DOM-Fe(II)} + H_2O_2 \rightarrow \text{DOM-Fe(III)} + {}^{\bullet}OH + OH^- \qquad \text{(Eq. SI-14)}$$

and produces hydroxyl radicals (Figure SI-2b). In the beginning of experiment, the calculated maximum rate of $^{\bullet}OH$ (1.05×10^{-9} mol L^{-1} s^{-1}) is similar to the measured rate of $^{\bullet}OH$ production ($R_f^{\bullet OH}(t_0)$ $=1.14 \times 10^{-9}$ mol L^{-1} s^{-1}; Figure 4d).

The simple kinetic model (Figure SI-2) can explain the initial rate of $^{\bullet}OH$ production in "Fe + KO_2" treatment, but it fails to describe the later kinetics of $^{\bullet}OH$ production and the cumulative amounts of produced $^{\bullet}OH$ (Figure 4d; 104 µmol L^{-1} $^{\bullet}OH$ in 168 h, Table 2). The simple kinetic model (Figure SI-2) predicts that the formation of $^{\bullet}OH$ stops in about three minutes, and produces cumulatively 3.8 µmol L^{-1} of $^{\bullet}OH$ with a final residual concentration of 0.8 µmol L^{-1} H_2O_2. The stoichiometry of $^{\bullet}OH$ production in the kinetic model (Figure SI-2) approximates iron-catalyzed Haber-Weiss process (Rush & Bielski, 1985):

$$HO_2^{\bullet} + H_2O_2 \xrightarrow{\text{Fe(II)/Fe(III)}} {}^{\bullet}OH + H_2O + O_2 \qquad \text{(Eq. SI-15a).}$$

When the formation of H_2O_2 through disproportionation (Eq. SI-4) is included in Eq. SI-15a, it becomes:

$$3\ HO_2^{\bullet} \xrightarrow{\text{Fe(II)/Fe(III)}} {}^{\bullet}OH + H_2O + 2\ O_2 \qquad \text{(Eq. SI-15b),}$$

The reaction Eq. SI-15 represents the theoretical maximum yield of $^{\bullet}OH$ ($^{\bullet}OH$/ 3 O_2^*) from superoxide through Fe catalysis, which is 4.3 µmol L^{-1} of $^{\bullet}OH$ from 13 µmol L^{-1} O_2^*. As the measured yield of $^{\bullet}OH$ (104 µmol L^{-1} $^{\bullet}OH$ in 168 h, Table 2) was 24-fold higher than the theoretical yield from $O_2^{\bullet-}$ (4.3 µmol L^{-1} $^{\bullet}OH$, Eq, SI-15b), the production of $^{\bullet}OH$ in the "Fe + KO_2" treatment must have included an autocatalytic process.

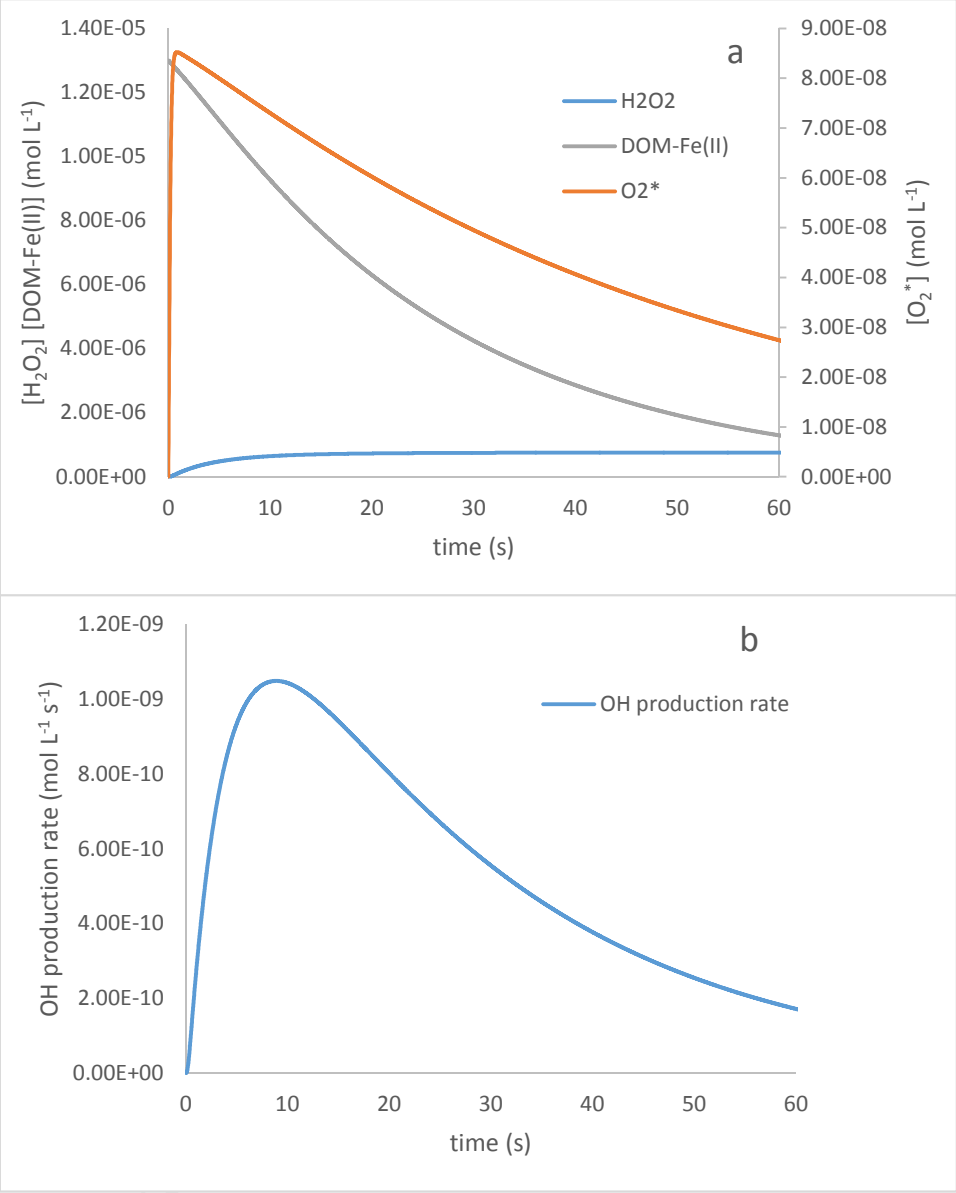

Figure SI-2. The calculated concentrations of DOM-Fe(II), H_2O_2 and O_2^* (a) and the production rate of hydroxyl radicals. The calculations on the oxidation of DOM-Fe(II) (Eq. SI-12), disproportionation of O_2^* (Eq. SI-4) and the Fenton reaction (Eq. SI-14).

Text SII: HPLC analysis for detecting coumarin and 7OH-coumarin

The HPLC system was a Shimadzu LC-30AD equipped with SIL-30AC autosampler, CTO-20AC column oven (set at 30 °C), DGU-20A5R degassing unit, SPD-M20A PDA detector and RF-20A XS fluorescence detector. Chromatographic runs were carried out with a reverse phase chromatography column Bridge Columns XBridge™ C18 (2.5 μm) in a gradient mode with a mixture of two eluents (A and B). Eluent A was 0.3% acetic acid with 99.7% ultrapure water, while B was 100% acetonitrile. The flow rate was 0.3 mL min^{-1}. The relevant elution gradients were: 10% of B from 0 to 0.5 min, then linear gradient to 45% of B from 0.5 to 6 min, followed by a fast linear gradient to 75% of B for 6–6.5 min; 75% of B was then kept from 6.5 to 9 min and then followed by a linear gradient to the initial condition 10% of B at 9.5 min, the same gradient was kept until 12.5 min for stabilizing the system. The injection volume was 5 μL. The first sample was run two times to make sure the gradient solvent was fully stabilized in the system. The retention times were 5.23 min for coumarin and 3.64 min for 7OH-coumarin. Quantification of the two compounds was carried out by means of the PDA detector for coumarin (absorption wavelength = 280 nm) and of the fluorescence detector for 7OH-coumarin (excitation wavelength = 320 nm; emission wavelength = 450 nm,).

Text SIII: Calculating the cumulative production of •OH radicals by using the transformation of coumarin into 7-hydroxycoumarin as a •OH probe reaction

The cumulative production of •OH radicals per unit of volume over a defined time ($[^{\bullet}OH]_{\Sigma}$, mol L^{-1}) was described as a definite integral over time:

$$[^{\bullet}OH]_{\Sigma} = \int_{t_0}^{t_1} R_f^{\bullet OH}(t)\, dt \qquad (Eq.\,S\mathrm{III}-1),$$

where t_0 and t_1 represent the time in the beginning of experiment and at the selected time t_1, respectively, and $R_f^{\bullet OH}(t)$ is the formation rate of •OH radicals at time t (mol L^{-1} s^{-1}).

$R_f^{\bullet OH}(t)$ was calculated from the scavenging rate of hydroxyl radicals. Because •OH radicals react with their scavengers almost at diffusion-controlled rates, the total scavenging rate of •OH at time t approximates $R_f^{\bullet OH}(t)$.When the formation and scavenging rates are nearly the same, the •OH concentration at time t approximates a steady-state. In the experimental solutions, the scavengers (see Scheme SIII-1) set the steady-state concentration of •OH radicals ($[^{\bullet}OH]_{s.s.}$) to:

$$[^{\bullet}OH]_{s.s.} = \frac{R_f^{\bullet OH}(t)}{k'_{Scav} + k_{Cou}^{\bullet OH}[Cou]_t + k_{7OHCou}^{\bullet OH}[7OHCou]_t} \qquad (Eq.\,S\mathrm{III}-2),$$

where $[Cou]_t$ and $[7OHCou]_t$ are the concentrations of coumarin and 7-hydroxycoumarin (7OH-coumarin) at time t, respectively (Figures SIII-1&2), and k'_{Scav} represents scavenging by the artificial lake water (Table SIII-1). k'_{Scav} accounted for the major scavengers of •OH in the artificial lake water: DOM (DOC = 11.35 mg C L^{-1}), chloride (*vide infra* for its concentration) and bicarbonate anions (4×10^{-6} mol L^{-1}), and thus $k'_{Scav} = k_{DOM}^{\bullet OH}DOC + k_{Cl^-}^{\bullet OH}[Cl^-] + k_{HCO_3^-}^{\bullet OH}[HCO_3^-]$. The modeling used the initial concentrations of Cl^- and HCO_3^- (Table SIII-1). In terms of DOM, we assumed that the reactions between hydroxyl radicals and DOM resulted primarily in the transformation products that reacted with hydroxyl radical like reported for DOM in literature (Westerhoff et al. 2007). Therefore, we used the initial concentrations of DOM in the calculations (Table SIII-1). The modeling also ignored the reactions of •OH radicals with the different coumarin degradation byproducts (P_2 and P_3 Scheme SIII-1), as well as those with the iron species, because we did not measure the

temporal variation of these compounds. However, this should not cause significant modeling errors, because these constituents had lower concentrations than the major scavenger DOM, making negligible their role in the total $^{\bullet}$OH radicals scavenging. The reaction rate constants were from literature: $k_{Cou}^{\bullet OH}$ = 5.6×10^9 L mol^{-1} s^{-1}; $k_{7OHCou}^{\bullet OH}$ = 6.1×10^9 L mol^{-1} s^{-1}; $k_{DOM}^{\bullet OH}$ = 1.9×10^4 L mg C^{-1} s^{-1}; $k_{HCO_3^-}^{\bullet OH}$ = 8.5×10^6 L mol^{-1} s^{-1} (Burgos Castillo et al., 2018; Buxton et al., 1988; Payá et al., 1992; Westerhoff et al., 2007). The value of $k_{Cl^-}^{\bullet OH}$ took into account the pH dependence of the $^{\bullet}$OH scavenging kinetics by Cl$^-$ (see Scheme SIII-1). At pH 2, the reaction between $^{\bullet}$OH and Cl$^-$ yields hypochlorous acid anion radicals (HOCl$^{\bullet-}$, k_1 = 4.3×10^9 L mol^{-1} s^{-1}, Buxton et al., 1988). In acidic conditions the protonation of HOCl$^{\bullet-}$ induces the formation of a chlorine atom (Cl$^{\bullet}$) and a water molecule (k_2 = 2.1×10^{10} L mol^{-1} s^{-1}, Jayson et al., 1973) making Cl$^-$ as an actual sink for $^{\bullet}$OH. At circumneutral and basic pH values, HOCl$^{\bullet-}$ dissociates back to $^{\bullet}$OH and Cl$^-$ (k_{-1} = 6.1×10^9 s^{-1}, Jayson et al., 1973). By considering these reactions and by reasonably applying the steady-state to the HOCl$^{\bullet-}$ concentration, the pH dependence of $k_{Cl^-}^{\bullet OH}$ can be described as $k_1 k_2 10^{-pH}(k_{-1} + k_2 10^{-pH})^{-1}$ (see also the paper by Jayson et al., 1973). Therefore, $k_{Cl^-}^{\bullet OH}$ □ 1.5×10^5 L mol^{-1} s^{-1} at pH 5. Chloride concentrations used in the model took into account all the Cl$^-$ sources (i.e. artificial lake water, $FeCl_3$, and HCl for the titration procedures) and were 1.84×10^{-4} mol L^{-1} ("control"), 7.4×10^{-3} mol L^{-1} ("Fe"), 1.62×10^{-2} mol L^{-1} ("KO_2") and 2.12×10^{-2} mol L^{-1} ("Fe+ KO_2").

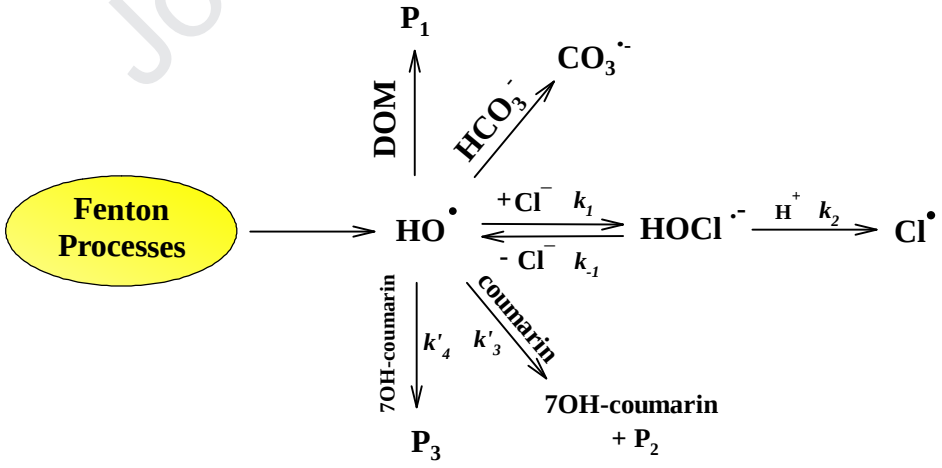

Scheme SIII-1. Simplified reaction scheme describing the formation and the scavenging pathways of $^{\bullet}$OH radicals in the experiment. 'P_i' refers to a general byproduct(s).

The transformation rate of 7OH-coumarin, $R_{\Delta}^{7OHCou}(t)$, was a master variable in the assessment of $R_f^{\bullet OH}(t)$. $R_{\Delta}^{7OHCou}(t)$ was defined as the difference between the formation rate (coumarin + $^{\bullet}$OH reaction) and the decay rate (7OH-coumarin + $^{\bullet}$OH reaction):

$$R_{\Delta}^{7OHCou}(t) = [^{\bullet}OH]_{s.s.}\{\eta_{7OHCou}^{Cou} k_{Cou}^{\bullet OH}[Cou]_t - k_{7OHCou}^{\bullet OH}[7OHCou]_t\} \qquad (Eq.SIII-3),$$

where η_{7OHCou}^{Cou} = 0.047 is the yield for the formation of 7OH-coumarin from the coumarin + $^{\bullet}$OH reaction (Burgos Castillo et al., 2018). By substituting Eq. SIII-2 in Eq. SIII-3, one obtains:

$$R_{\Delta}^{7OHCou}(t) = \frac{R_f^{\bullet OH}(t)\{\eta_{7OHCou}^{Cou} k_{Cou}^{\bullet OH}[Cou]_t - k_{7OHCou}^{\bullet OH}[7OHCou]_t\}}{k'_{Scav} + k_{Cou}^{\bullet OH}[Cou]_t + k_{7OHCou}^{\bullet OH}[7OHCou]_t} \qquad (Eq.SIII-4)$$

By rearranging Eq. SIII-4, the expression for $R_f^{\bullet OH}(t)$ will be:

$$R_f^{\bullet OH}(t) = \frac{R_{\Delta}^{7OHCou}(t)\{k'_{Scav} + k_{Cou}^{\bullet OH}[Cou]_t + k_{7OHCou}^{\bullet OH}[7OHCou]_t\}}{\{\eta_{7OHCou}^{Cou} k_{Cou}^{\bullet OH}[Cou]_t - k_{7OHCou}^{\bullet OH}[7OHCou]_t\}} \qquad (Eq.SIII-5)$$

$R_{\Delta}^{7OHCou}(t)$ was assessed as the first derivative ($d[7OHCou]_t dt^{-1}$) of a function that described the temporal development of $[7OHCou]_t$ in the treatments. In order to determine $d[7OHCou]_t dt^{-1}$, a kinetic equation SIII-6 (the curves in Figure SIII-1) was fitted on the measured concentrations of 7OH-coumarin during the course of experiment (the squares in Figure SIII-1).

$$[7OHCou]_t = \frac{k'_3 a}{k'_4 - k'_3}(e^{-k'_3 t} - e^{-k'_4 t}) \qquad (Eq.SIII-6)$$

where k'_3 and k'_4 are the pseudo-first order rate constants for the reactions $Cou \rightarrow 7OHCou$ and $7OHCou \rightarrow P_3$, respectively (Scheme SIII-1), and a is a concentration parameter. The values of $R_{\Delta}^{7OHCou}(t)$ were graphically computed as the slope of the tangent line to the curves shown in Figure SIII-1 at several reaction times shown in Figure 4.

For the calculation of $R_f^{\bullet OH}(t)$, Eq. SIII-5 received the values of $R_{\Delta}^{7OHCou}(t)$, $[7OHCou]_t$ (Figure SIII-1) and $[Cou]_t$ (Figure SIII-2) at the selected times (the reaction times in Figure

4). The decreasing trend in $R_f^{\bullet OH}(t)$ at the selected times (the squares in Figure 4) was described by an exponential equation (the curves in Figure 4):

$$R_f^{\bullet OH}(t) = R_f^{\bullet OH}(t_0)\, e^{-kt} \qquad (Eq.\ \text{SIII-7}),$$

where $R_f^{\bullet OH}(t_0)$ is the rate of hydroxyl radicals formation in the beginning of experiment (nmol L^{-1} s^{-1}) and k (s^{-1}) describes the degree of exponential loss in $R_f^{\bullet OH}(t)$. In the "Fe+KO_2"-treatment, $R_f^{\bullet OH}(t)$ decreased initially exponentially but plateaued later (Figure 4d) and therefore the kinetics was described by:

$$R_f^{\bullet OH}(t) = R_f^{\bullet OH}(t_0)\, e^{-kt} + R_f^{\bullet OH}\left(t_{plateau}\right) \qquad (Eq.\ \text{SIII-8}),$$

where $R_f^{\bullet OH}\left(t_{plateau}\right)$ is the rate at the plateau. Table SIII-1 shows the values of the relevant parameters of Eq. SIII-7&8.

Finally, the $[^{\bullet}OH]_{\Sigma}$ values were calculated by solving the integral of these fitting functions as in Eq. SIII-1.

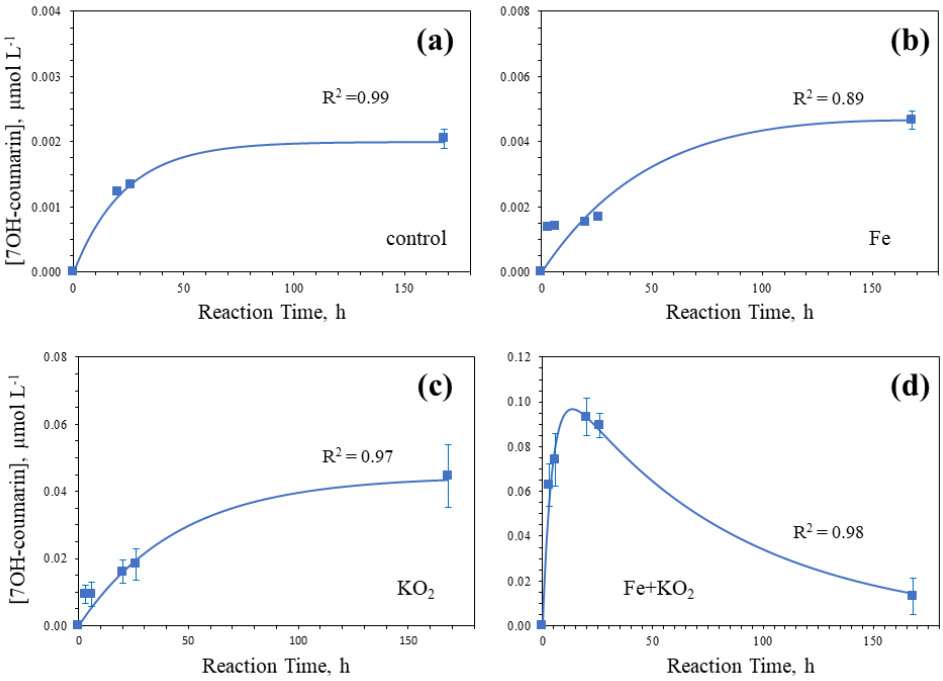

Figure SIII-1. The measured concentrations of 7-hydroxycoumarin (7OH-coumarin) (■) and the kinetic fitting on the measured data (blue lines). The error bars represent data standard deviations. The

R^2 parameter shows the goodness of the fit. See Eq. S6 for the general form of the fitting functions. Note, the differences in the scale of Y-axis among the panels.

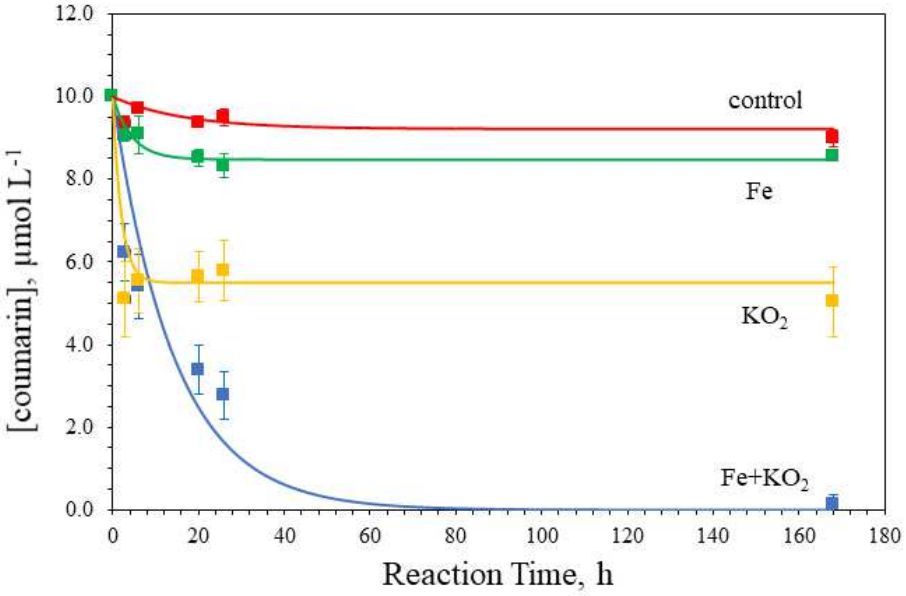

Figure SIII-2. Concentration profiles of coumarin observed in the different treatments. The error bars represent the standard deviations of the measured coumarin concentrations (squares). Data were fitted with the equation $[Cou]_t = C + A\exp(-Bt)$ (lines). In the case "Fe+KO_2", C = 0 (blue curve).

Table SIII-1. Fitting parameters obtained by interpolating the $R_f^{\bullet OH}(t)$ data with Eq. SIII-7 & SIII-8. The R^2 value shows the goodness of the fit.

Treatment	$\boldsymbol{R_f^{\bullet OH}(t_0)}$, **nmol L^{-1} s^{-1}**	$\boldsymbol{k}$, **s^{-1}**	$\boldsymbol{R_f^{\bullet OH}(t_{plateau})}$, **nmol L^{-1} s^{-1}**	**R^2**
control	$(3.074\pm0.085)\times10^{-3}$	$(1.340\pm0.067)\times10^{-5}$	0	0.99
Fe	$(3.361\pm0.221)\times10^{-3}$	$(5.668\pm0.804)\times10^{-6}$	0	0.97
KO_2	$(3.894\pm0.225)\times10^{-2}$	$(3.454\pm0.466)\times10^{-6}$	0	0.95
Fe+KO_2	$(9.910\pm0.384)\times10^{-1}$	$(8.745\pm0.701)\times10^{-5}$	$(1.523\pm0.137)\times10^{-1}$	0.99

Text SIV: Modeling $O_2^{\bullet-}$ photoproduction in lake water.

Superoxide ($O_2^{\bullet-}$) photochemical production in surface waters can be related to the formation of hydrogen peroxide (H_2O_2) from irradiated chromophoric dissolved organic matter (CDOM). Indeed, H_2O_2 is photoproduced by CDOM through a mechanism that would involve the reduction of dioxygen (O_2) to superoxide $O_2^{\bullet-}$ by O_2-reducing intermediates that are generated by intramolecular electron transfer from CDOM short-lived excited states of electron donors (probably phenols) to ground-state acceptors (most likely quinone-like moieties) (Zhang et al., 2012). In the presence of a high content of electro-donating phenols, the excited triplet states of CDOM can be involved in $O_2^{\bullet-}$ photoproduction as well (Zhang et al., 2014). Then $O_2^{\bullet-}$ can undergo dismutation, which can occur via three main pathways: *(i)* uncatalyzed dismutation ($O_2^{\bullet-}$ + $HO_2^{\bullet}$), *(ii)* DOM-catalyzed dismutation ('DOM' means dissolved organic matter) and *(iii)* dismutation catalyzed by organometallic compounds containing Fe, Cu and Mn (Goldstone & Voelker, 2000; Ma et al., 2019). Among these processes, the DOM-catalyzed dismutation of $O_2^{\bullet-}$ into H_2O_2 + O_2 can play the main scavenging role of $O_2^{\bullet-}$ in inland surface waters (Ma et al., 2019). As far as the stoichiometry of $O_2^{\bullet-}$ dismutation is concerned, previous works have determined the ratio H_2O_2:$O_2^{\bullet-}$ for different DOM type (Goldstone & Voelker, 2000; Powers & Miller, 2016), showing that the ratio should be □0.5 for DOM typically occurring in inland waters, while it would decrease down to □0.25 for seawater and open ocean (Powers & Miller, 2016). Here, we adopted the former values in order to model superoxide photoproduction in lake water.

By doubling the H_2O_2 photoproduction rate from irradiated CDOM (R_{H2O2}^{CDOM}), one can get the $O_2^{\bullet-}$ photoformation rate, $R_{O_2^{\bullet-}}^{CDOM} = 2R_{H2O2}^{CDOM} = 2\Phi_{H2O2}^{CDOM} P_{a,CDOM}$. Φ_{H2O2}^{CDOM} is the polychromatic apparent quantum yield (pAQY) of H_2O_2 formation from irradiated CDOM, while $P_{a,CDOM}$ is the total photon flux absorbed by CDOM (or photons absorption rate, Einstein L^{-1} s^{-1}). Φ_{H2O2}^{CDOM} has been measured by Zhang et al. (2012) for several DOM samples, such as Suwannee River humic and fulvic acids, a lignin-like material and a river water sample. The average value for these materials is □5.9x10^{-4}. $P_{a,CDOM}$ is a function of the light absorption properties of CDOM, water depth and chemical composition, namely $P_{a,CDOM} = \int_{\lambda 1}^{\lambda 2} p^0(\lambda) \frac{Abs_\lambda^{CDOM}}{Abs_\lambda^{tot}} \left[1 - 10^{-Abs_\lambda^{tot}}\right] d\lambda$. Abs_λ^{tot} is the total absorbance of water that takes into account the water depth and the Lambert-Beer absorbance of the main light-absorbing species, Abs_λ^{CDOM} is the absorbance of CDOM and $p^0(\lambda)$ is the spectral solar photon flux (Einstein L^{-}

^{1} s^{-1} nm^{-1}). To evaluate $P_{a,CDOM}$ one has to know all these parameters, which are particular features of the considered water body. The APEX software (*Aqueous Photochemistry of Environmentally occurring Xenobiotics*; Bodrato & Vione, 2014) allows to indirectly assess $P_{a,CDOM}$. Indeed, APEX models the direct and indirect photochemistry of water pollutants in well-mixed surface waters (e.g., Carena et al., 2017), such as the lake epilimnion during stratification in summertime, as well as the steady-state concentrations of the main *Photochemically Produced Reactive Intermediates* (PPRIs), namely hydroxyl and carbonate radicals ($HO^{\bullet}$ and $CO_3^{\bullet-}$, respectively), the excited triplet states of CDOM (^{3}CDOM*) and singlet oxygen ($^{1}O_2$).

To assess the PPRIs steady-state concentrations, APEX requires as input data the chemical and photochemical features of the water body, namely the photosensitizers concentration (NO_3^-, NO_2^- and CDOM, the latter quantified by means of the dissolved organic carbon DOC), the water absorption spectrum (which is computed based on the input DOC value) and the water depth. For the detailed description of the model, see the APEX User Guide available for free in Bodrato and Vione (2014). The software output data are averaged over the entire water column depth. $P_{a,CDOM}$ can be determined by modeling the steady-state concentration of ^{3}CDOM*, $[^3CDOM^*]_{s.s.} = \Phi_{3CDOM*}^{CDOM} P_{a,CDOM} (k_{3CDOM*})^{-1}$, where Φ_{3CDOM*}^{CDOM} = 1.28x10^{-3} is the ^{3}CDOM* formation pAQY and k_{3CDOM*} = 5x10^{5} s^{-1} is the rate constant of the ^{3}CDOM* scavenging by the reaction with O_2 (that forms $^{1}O_2$). As a consequence, $R_{O_2^{\bullet-}}^{CDOM} = 2R_{H2O2}^{CDOM} = 2\Phi_{H2O2}^{CDOM} [^3CDOM^*]_{s.s.} k_{3CDOM*} (\Phi_{3CDOM*}^{CDOM})^{-1}$. Note that this equation refers to the direct photoproduction of $O_2^{\bullet-}$ upon sunlight absorption by CDOM. It does not take into account those reactions occurring in surface waters that indirectly photoproduce $O_2^{\bullet-}$ as an intermediate, such as, for example, the DOM photodegradation, the nitrate/nitrite photolysis, and the xenobiotics degradation. Moreover, note that here $R_{O_2^{\bullet-}}^{CDOM} \propto [^3CDOM^*]_{s.s.}$ is only due to $P_{a,CDOM}$ -evaluation purposes, and it does not mean that ^{3}CDOM* is mechanistically linked to $O_2^{\bullet-}$ photoproduction (Zhang et al., 2014; Zhang et al., 2012).

Figure SIV-1 shows $R_{O_2^{\bullet-}}^{CDOM}$ as a function of water depth and DOC. It must be pointed out that the $R_{O_2^{\bullet-}}^{CDOM}$ strongly depends upon O_2 concentration (Zhang et al., 2012). Unfortunately, APEX does not consider O_2 as an input variable and thus the results showed in Fig. SIV-1 are relevant for well oxygenated (saturated) waters.

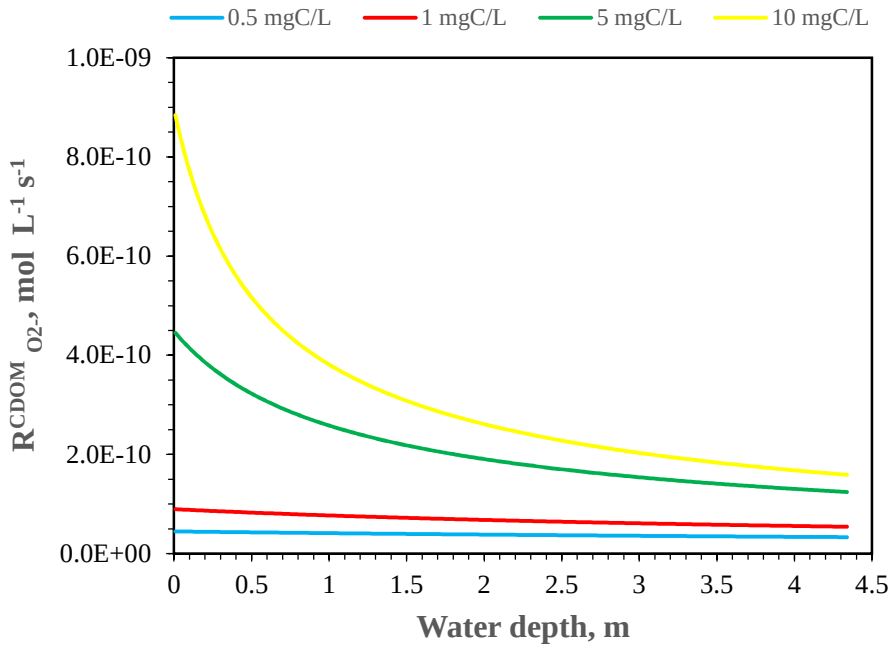

Figure SIV-1. Superoxide photoproduction rate in a temperate lake (45°N) as a function of water depth and DOC, during the 15th of July at 09 am or 03 pm. Other water chemical composition parameters were 1.0x10^{-4} mol L^{-1} NO_3^-, 1.0x10^{-6} mol L^{-1} NO_2^-, 1.0x10^{-3} mol L^{-1} alkalinity and pH 7. Note that the data are averaged over the entire water column.

The solar spectrum used for the modeling (i.e., $p^0(\lambda)$) refers to the Sun spectrum reaching the water surface on the 15th of July at mid-latitudes (45°N) at solar noon ± 3h, that is at 09 a.m. or 03 p.m., with 22 W m^{-2} UV irradiance. This is roughly representative of a daily average solar spectrum. Such a condition allows to define the Summer Sunny Day (SSD), which is the time unit adopted by APEX to describe, for instance, the photochemical half-life time of water pollutants. SSD = 10 h of continuous solar irradiation with 22 W m^{-2} UV irradiance.

By so doing, one can assess how many hours of solar irradiation are required to directly photoproduce 13 µmol $O_2^{\bullet-}$ L^{-1} in a lake, without considering the daily fluctuations of solar irradiance. $R_{O_2^{\bullet-}}^{CDOM}$ varied from 4.5x10^{-11} to 9x10^{-10} mol L^{-1} s^{-1} and, as a consequence, 13 µmol $O_2^{\bullet-}$ L^{-1} are photoproduced in a time interval ranging from ≈4 h to ≈8.5 SSD in the first meter of a lake (Fig. SIV-2). The modeled $R_{O_2^{\bullet-}}^{CDOM}$ for 0.5 and 1 mgC L^{-1} are quite similar to the superoxide formation rates that can be calculated from the H_2O_2 production rates measured by García et al. (2019) during lab irradiation of Andean shallow lakes with similar DOC values. However, these results can be considered as minimum limit values of

superoxide photoproduction, because the ratio H_2O_2:$O_2^{\bullet-}$ could be lower than the adopted one (i.e., 0.5).

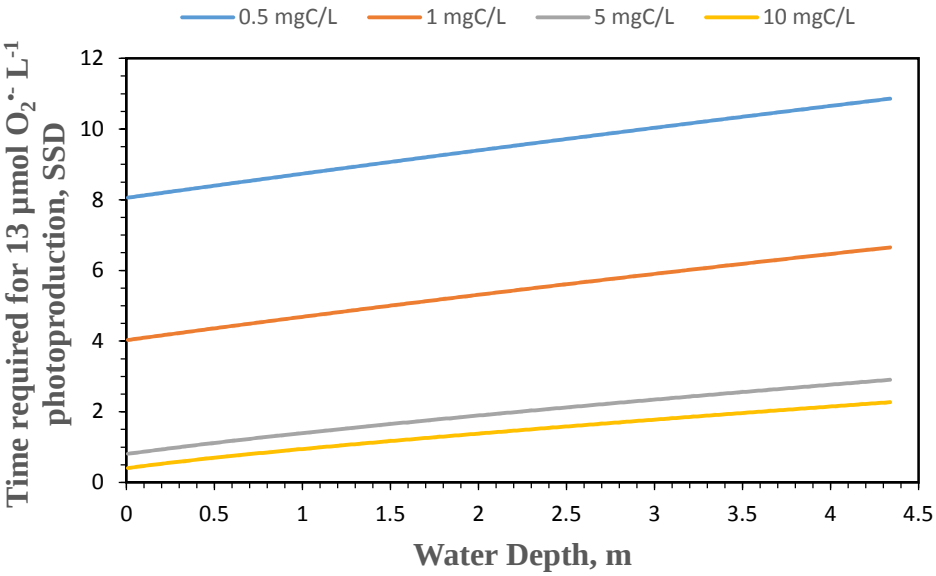

Figure SIV-2. Time required for 13 µmol $O_2^{\bullet-}$ L^{-1} photoproduction in a temperate lake (45°N) as a function of water depth and DOC, during the 15th of July at 09 am or 03 pm. Further water chemical composition parameters were $1.0x10^{-4}$ mol L^{-1} NO_3^-, $1.0x10^{-6}$ mol L^{-1} NO_2^-, $1.0x10^{-3}$ mol L^{-1} alkalinity and pH 7. Note that the data are averaged over the entire water column.

References

Bielski, B. H. J., Cabelli, D. E., & Arudi, R. L. (1985). Reactivity of HO2/O2– radicals in aqueous solution. *Journal of Physical Chemistry Reference Data*, *14*(4), 1041–1100.

Bodrato, M., & Vione, D. (2014). APEX (Aqueous Photochemistry of Environmentally occurring Xenobiotics): A free software tool to predict the kinetics of photochemical processes in surface waters. *Environmental Sciences: Processes and Impacts*, *16*(4), 732–740. https://doi.org/10.1039/c3em00541k

Burgos Castillo, R. C., Fontmorin, J. M., Tang Walter, Z., Xochitl, D. B., & Mika, S. (2018). Towards reliable quantification of hydroxyl radicals in the Fenton reaction using chemical probes. *RSC Advances*, *8*(10), 5321–5330. https://doi.org/10.1039/c7ra13209c

Buxton, G. V., Greenstock, C. L., Helman, W. P., & Ross, A. B. (1988). Critical Review of rate constants for reactions of hydrated electrons, hydrogen atoms and hydroxyl radicals (· OH/· O−in Aqueous Solution. *Journal of Physical and Chemical Reference Data*, *17*(2), 513–886. https://doi.org/10.1063/1.555805

Carena, L., Minella, M., Barsotti, F., Brigante, M., Milan, M., Ferrero, A., et al. (2017). Phototransformation of the Herbicide Propanil in Paddy Field Water. *Environmental Science and Technology*, *51*(5), 2695–2704. https://doi.org/10.1021/acs.est.6b05053

Coble, P. G., Green, S. A., Blough, N. V., & Gagosian, R. B. (1990). Characterization of dissolved organic matter in the Black Sea by fluorescence spectroscopy. *Nature*, *348*(6300), 432–435. https://doi.org/10.1038/348432a0

Coble, P. G., Del Castillo, C. E., & Avril, B. (1998). Distribution and optical properties of CDOM in the Arabian Sea during the 1995 Southwest Monsoon. *Deep Sea Research Part II: Topical Studies in Oceanography*, *45*(10–11), 2195–2223. https://doi.org/10.1016/S0967-0645(98)00068-X

Cory, R. M., McKnight, D. M., And, R. M. C., & McKnight, D. M. (2005). Fluorescence spectroscopy reveals ubiquitous presence of oxidized and reduced quinones in dissolved organic matter. *Environmental Science & Technology*, *39*(21), 8142–8149. https://doi.org/10.1021/ES0506962

Fujii, M., & Otani, E. (2017). Photochemical generation and decay kinetics of superoxide and hydrogen peroxide in the presence of standard humic and fulvic acids. *Water Research*, *123*, 642–654. https://doi.org/10.1016/j.watres.2017.07.015

García, P. E., Queimaliños, C., & Diéguez, M. C. (2019). Natural levels and photo-production rates of

hydrogen peroxide (H2O2) in Andean Patagonian aquatic systems: Influence of the dissolved organic matter pool. *Chemosphere*, 550–557. https://doi.org/10.1016/j.chemosphere.2018.10.179

Garg, S., Rose, A. L., & Waite, T. D. (2007). Superoxide mediated reduction of organically complexed iron(III): Comparison of non-dissociative and dissociative reduction pathways. *Environ. Sci. Technol.*, *41*(9), 3205–3212. https://doi.org/10.1021/ES0617892

Goldstone, J. V., & Voelker, B. M. (2000). Chemistry of superoxide radical in seawater: CDOM associated sink of superoxide in coastal waters. *Environmental Science and Technology*, *34*(6), 1043–1048. https://doi.org/10.1021/es9905445

Gu, C., Wang, J., Guo, M., Sui, M., Lu, H., & Liu, G. (2018). Extracellular degradation of tetrabromobisphenol A via biogenic reactive oxygen species by a marine Pseudoalteromonas sp. *Water Research*, *142*, 354–362. https://doi.org/10.1016/j.watres.2018.06.012

Jayson, G. G., Parsons, B. J., & Swallow, A. J. (1973). Some simple, highly reactive, inorganic chlorine derivatives in aqueous solution. Their formation using pulses of radiation and their role in the mechanism of the Fricke dosimeter. *Journal of the Chemical Society, Faraday Transactions 1: Physical Chemistry in Condensed Phases*, *69*, 1597–1607. https://doi.org/10.1039/F19736901597

Kothawala, D. N., Stedmon, C. A., Muller, R. A., Weyhenmeyer, G. A., Köhler, S. J., & Tranvik, L. J. (2014). Controls of dissolved organic matter quality: evidence from a large-scale boreal lake survey, *20*, 1101–1114. https://doi.org/10.1111/gcb.12488

Louit, G., Foley, S., Cabillic, J., Coffigny, H., Taran, F., Valleix, A., et al. (2005). The reaction of coumarin with the OH radical revisited: Hydroxylation product analysis determined by fluorescence and chromatography. *Radiation Physics and Chemistry*, *72*(2–3), 119–124. https://doi.org/10.1016/j.radphyschem.2004.09.007

Ma, J., Zhou, H., Yan, S., & Song, W. (2019). Kinetics studies and mechanistic considerations on the reactions of superoxide radical ions with dissolved organic matter. *Water Research*, *149*, 56–64. https://doi.org/10.1016/J.WATRES.2018.10.081

Parlanti, E., Wörz, K., Geoffroy, L., & Lamotte, M. (2000). Dissolved organic matter fluorescence spectroscopy as a tool to estimate biological activity in a coastal zone submitted to anthropogenic inputs. *Organic Geochemistry*, *31*(12), 1765–1781. https://doi.org/10.1016/S0146-6380(00)00124-8

Payá, M., Halliwell, B., & Hoult, J. R. S. (1992). Interactions of a series of coumarins with reactive oxygen species. Scavenging of superoxide, hypochlorous acid and hydroxyl radicals. *Biochemical Pharmacology*, *44*(2), 205–214. https://doi.org/10.1016/0006-2952(92)90002-Z

Pignatello, J. J., Oliveros, E., & MacKay, A. (2006). Advanced oxidation processes for organic contaminant destruction based on the fenton reaction and related chemistry. *Critical Reviews in Environmental Science and Technology*, *36*(1), 1–84. https://doi.org/10.1080/10643380500326564

Powers, L. C., & Miller, W. L. (2016). Apparent quantum efficiency spectra for superoxide photoproduction and its formation of hydrogen peroxide in natural waters. *Frontiers in Marine Science*, *3*(NOV). https://doi.org/10.3389/fmars.2016.00235

Rush, J. D., & Bielski, B. H. J. (1985). Pulse radiolytic studies of the reaction of perhydroxyl/superoxide O2- with iron(II)/iron(III) ions. The reactivity of HO2/O2- with ferric ions and its implication on the occurrence of the Haber-Weiss reaction. *The Journal of Physical Chemistry*, *89*(23), 5062–5066. https://doi.org/10.1021/j100269a035

Stedmon, C. A., Markager, S., & Bro, R. (2003). Tracing dissolved organic matter in aquatic environments using a new approach to fluorescence spectroscopy. *Marine Chemistry*, *82*(3–4), 239–254. https://doi.org/10.1016/S0304-4203(03)00072-0

Westerhoff, P., Mezyk, S. P., Cooper, W. J., & Minakata, D. (2007). Electron pulse radiolysis determination of hydroxyl radical rate constants with Suwannee river fulvic acid and other dissolved organic matter isolates. *Environmental Science and Technology*, *41*(13), 4640–4646. https://doi.org/10.1021/es062529n

Wuttig, K., Heller, M. I., & Croot, P. L. (2013). Reactivity of Inorganic Mn and Mn Desferrioxamine B with O2 , O2 – , and H2O2 in Seawater. *Environmental Science & Technology*, *47*(18), 10257–10265. https://doi.org/10.1021/es4016603

Zhang, X., Yin, S., Li, Y., Zhuang, H., Li, C., & Liu, C. (2014). Comparison of greenhouse gas emissions from rice paddy fields under different nitrogen fertilization loads in Chongming Island, Eastern China. *Science of The Total Environment*, *472*, 381–388. https://doi.org/10.1016/J.SCITOTENV.2013.11.014

Zhang, Yi, Del Vecchio, R., & Blough, N. V. (2012). Investigating the Mechanism of Hydrogen Peroxide Photoproduction by Humic Substances. *Environmental Science & Technology*, *46*(21), 11836–11843. https://doi.org/10.1021/es3029582

Zhang, Yunlin, van Dijk, M. A., Liu, M., Zhu, G., & Qin, B. (2009). The contribution of phytoplankton degradation to chromophoric dissolved organic matter (CDOM) in eutrophic shallow lakes: Field and experimental evidence. *Water Research*, *43*(18), 4685–4697. https://doi.org/10.1016/j.watres.2009.07.024

Declaration of competing interest

The authors declare no competing financial interest.